*2156–2172* *Nucleic Acids Research, 2020, Vol. 48, No. 4* *Published online 11 January 2020*
*doi: 10.1093/nar/gkz1226*

# Structural basis for osmotic regulation of the DNA binding properties of H-NS proteins

**Liang Qin[1,2,†], Fredj Ben Bdira[1,2,*,†], Yann G.J. Sterckx[3], Alexander N. Volkov[4,5], Jocelyne Vreede[6], Gabriele Giachin[7], Peter van Schaik[1,2], Marcellus Ubbink[1] and Remus T. Dame[1,2,*]**

[1]Department of Macromolecular Biochemistry, Leiden Institute of Chemistry, Einsteinweg 55, 2333 CC Leiden, the Netherlands, [2]Centre for Microbial Cell Biology, Leiden University, Einsteinweg 55, 2333CC Leiden, the Netherlands, [3]Laboratory of Medical Biochemistry, University of Antwerp, Campus Drie Eiken, University Square 1, 2610 Wilrijk, Belgium, [4]VIB-VUB Structural Biology Research Center, Pleinlaan 2, 1050 Brussels, Belgium, [5]Jean Jeener NMR Centre, VUB, Pleinlaan 2, 1050 Brussels, Belgium, [6]Department of Computational Chemistry, Van't Hoff Institute for Molecular Sciences, University of Amsterdam Science Park 904, 1098 XH Amsterdam, the Netherlands and [7]Structural Biology Group, European Synchrotron Radiation Facility (ESRF), Grenoble, France

Received September 06, 2019; Revised November 29, 2019; Editorial Decision December 17, 2019; Accepted December 19, 2019

## ABSTRACT

**H-NS proteins act as osmotic sensors translating changes in osmolarity into altered DNA binding properties, thus, regulating enterobacterial genome organization and genes transcription. The molecular mechanism underlying the switching process and its conservation among H-NS family members remains elusive. Here, we focus on the H-NS family protein MvaT from *Pseudomonas aeruginosa* and demonstrate experimentally that its protomer exists in two different conformations, corresponding to two different functional states. In the half-opened state (dominant at low salt) the protein forms filaments along DNA, in the fully opened state (dominant at high salt) the protein bridges DNA. This switching is a direct effect of ionic strength on electrostatic interactions between the oppositely charged DNA binding and N-terminal domains of MvaT. The asymmetric charge distribution and intramolecular interactions are conserved among the H-NS family of proteins. Therefore, our study establishes a general paradigm for the molecular mechanistic basis of the osmosensitivity of H-NS proteins.**

## INTRODUCTION

Bacteria are frequently exposed to changes in their extracellular *milieu*. Key to their survival is to adapt quickly to these environmental fluctuations by adjusting their cellular machinery, enabling them to operate optimally under the new conditions, and to acquire new competencies through horizontal gene transfer (HGT) (1). These adaptation mechanisms are regulated by the bacterial genome, the dynamic organisation of which modulates access to the genetic material to adapt and fine-tune gene expression and for incorporation of DNA of foreign origin (2).

The Histone-like nucleoid structuring (H-NS) protein is a key regulator of the dynamic bacterial genome (3,4). The protein is conserved among enterobacteria and plays a determinant role in their nucleoid architecture. Generally, this protein acts as repressor of transcription, silencing the expression of many different genes and operons. Often the genes and operons targeted by H-NS family proteins are regulated by environmental conditions such as osmolarity, pH and temperature (5–7). Additionally, H-NS family members have the unique ability to 'switch off' xenogeneic genes, often in pathogens, to suppress their detrimental effect on bacterial fitness, until external conditions require expression (8–11). To similar effect, H-NS has been shown to silence spurious transcription at intragenic promoters in *Escherichia coli* (12).

H-NS is expressed at high levels (>20 000 copies per cell). The protein binds non-specifically to DNA, but has a preference towards genomic regions with high AT content (10,11,13), containing specific six contiguous steps (14). DNA binding typically initiates at such high-affinity sites on the DNA (15). This step is followed by oligomerization of the protein, forming lateral nucleoprotein filaments (16), which stiffens DNA (17). Under appropriate conditions the protein can mediate bridge formation between this filament and a second DNA duplex (18–22).

*To whom correspondence should be addressed. Tel: +31 71 5275605; Email: rtdame@chem.leidenuniv.nl
Correspondence may also be addressed to Fredj Ben Bdira. Email: f.ben.bdira@chem.leidenuniv.nl
†The authors wish it to be known that, in their opinion, the first two authors should be regarded as Joint First Authors.

The current paradigm is that divalent ions drive the transition between lateral H-NS–DNA filaments and bridged DNA-H-NS–DNA complexes, without dissociation of the protein from the DNA (20,23). This switching between the two types of complexes is believed to be the mechanistic basis of the role of H-NS proteins in bacterial nucleoid organisation and transcription regulation (20,23,24). Nonetheless, the molecular basis that governs this phenomenon is still controversial. Previously published molecular dynamics of H-NS, indicated that the switch between the two DNA binding modes involves a change from a half-open (also referred to as a closed conformation) to an open conformation driven by $MgCl_2$ (20). These conformational changes are modulated by the interactions between the N-terminal domain of H-NS and its C-terminal DNA binding domain (DBD). Mutagenesis at the interface of these domains generated an H-NS variant no longer sensitive to $MgCl_2$, which can form filaments and bridge DNA. Recently, these interactions were confirmed by Arold *et al.* using H-NS truncated domains (25). However, it was claimed that these interactions could not occur unless H-NS oligomerization is abolished by temperature. These discrepancies in conclusions arise presumably from the lack of experimental structural information on the full-length protein in solution.

H-NS family members share a conserved fold topology, with a C-terminal DBD and an N-terminal domain connected via a flexible linker (26,27). The structural unit of an H-NS nucleoprotein filament is a dimer (also called protomer) formed through the N-terminal dimerization sites of two monomers (site 1), which further oligomerize through a secondary oligomerization site (site 2) (28) (Figure 1A,B). Multiple studies have revealed the structures of H-NS truncated domains including the dimerization sites and the DBD from different bacteria (14,29–31). Meanwhile, no structure of the full-length protein is available. The structure of the N-terminal domain oligomer (1–83) of the *Salmonella typhimurium* H-NS C21S mutant was solved by crystallography (32). These studies revealed a helical scaffold of a head–head and tail–tail protomer organisation, suggesting structural models involving that type of H-NS arrangement in both lateral H-NS–DNA filaments and bridged DNA–H-NS–DNA complexes.

Early studies by liquid state NMR on full length H-NS from *E. coli* and *S. typhimurium* have shown that resonances of the N-terminal domain residues were missing in the protein heteronuclear single quantum coherence (HSQC) NMR spectrum (29,33). A similar observation was made using solid-state NMR in which case only 33% of the protein spectrum was assigned (34). These difficulties were attributed to the inherent dynamics and structural heterogeneity of the system. Thus, owing to their flexibility and the large size of their self-assembled complexes, the characterization of the conformational landscape of full-length H-NS proteins and its contribution to functional regulation remains a challenge. In this work we have overcome these constraints by using an abridged structural version of H-NS, MvaT from *P. aeruginosa*, in which we scrutinized its protomer structural/function relationship in response to changes in the surrounding ionic strength.

MvaT is a functional homologue of H-NS that regulates the expression of ∼350 genes including the genes responsible for virulence (35) and biofilm formation (36,37). Like other members of the H-NS family, oligomerization of MvaT along DNA is required for its gene silencing activity (38,39) and ability to stiffen and bridge DNA duplexes (19,39).

Here, we have combined integrative structural biology methods and (single-molecule) biochemical assays to decipher the structural changes in MvaT that drive the switch between its DNA stiffening and bridging activities under the influence of different salt conditions. These structural changes appear to be conserved within the H-NS family of proteins. Our studies thus provide a fundamental answer on how H-NS family members respond to changes in the osmotic environment to modulate their DNA binding modes, and hence to regulate bacterial nucleoid organisation and gene expression.

## MATERIALS AND METHODS

### Construction of expression vectors and mutagenesis

The MvaT coding gene from P. *aeruginosa* and its DBD (residues 76–124) were subcloned into pET30b vector without and with C-terminal 6× His-tag, respectively, using Gibson assembly (40). The Gibson assembly primers were purchased from Sigma-Aldrich. Mutated MvaT derivatives were generated using the same approach. Accuracy of the cloned sequences was confirmed by DNA sequencing.

### DNA substrates

All tethered particle motion and pull-down bridging assay experiments were performed using a random, AT-rich, 685 bp (32% GC) DNA substrate. The DNA substrate was generated by PCR and the products were purified using a GenElute PCR Clean-up kit (Sigma-Aldrich). If required, DNA was $^{32}$P-labeled as described previously (20). For the electrophoretic mobility shift assay an AT-rich 200 bp (32%GC) was generated using the same procedure.

The oligonucleotides to generate the 12 bp DNA duplex d(CGCATATATGCG) were purchased from Sigma Aldrich. The lyophilized oligonucleotides were solubilized in 20 mM Bis–Tris Buffer, 50 mM or 300 mM KCl, pH 6, combined and hybridized by heating to 98°C for 3 min, followed by slow cooling down to room temperature. The 12 bp DNA duplex was used for NMR titration of the MvaT dimer and DBD.

### Protein expression and purification

*Escherichia coli* BL21 competent cells were transformed with the MvaT pET30b vector and cultured in LB medium. For $^{15}$N $^{13}$C or $^{15}$N isotopic labeling, the transformed cells were first cultured in 2 mL LB medium and then transferred into 50 mL of inoculation culture in M9 medium (comprising the required isotopes) for incubation overnight at 37°C. The inoculation culture was diluted in 1 L M9 medium and was incubated at 37°C until it reached an $OD_{600}$ ≈0.6. MvaT production was induced by adding 100 μM of isopropyl β-D-1-thiogalactopyranoside (IPTG) and the culture was incubated overnight at 20°C. The next day cells

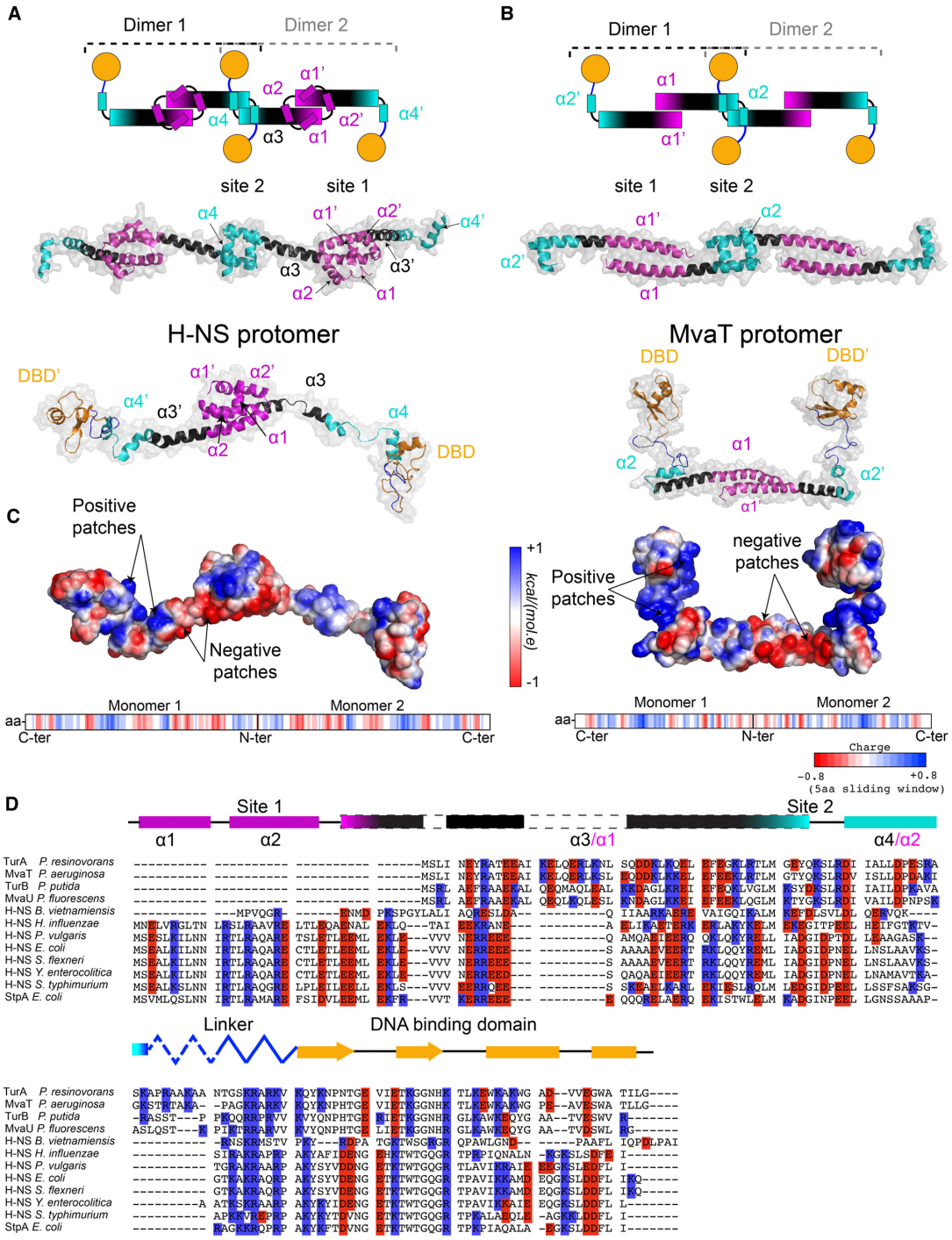


**Figure 1.** Fold topology and charged residue/charge distributions of H-NS family proteins. (**A**) N-terminal dimerization sites of long H-NS family members. The upper panel depicts a schematic representation of the long H-NS oligomer. The dimerization sites (site 1) are shown in magenta and the oligomerization sites (site 2) in cyan. The DNA binding domain is shown in orange sphere and the linker region in blue. In the middle panel is the H-NS N-terminal domain crystal structure (1–83) (PDB ID: 3NR7) (32). Site 1 and Site 2 helices are colored and labelled as in the upper panel. In the lower panel is the H-NS protomer structural model adapted from our earlier MD simulation studies (20). (**B**) N-terminal dimerization sites of short H-NS family members. The upper panel depicts a schematic representation of the short H-NS oligomer. In the middle panel is the TurB N-terminal domain crystal structure (1–64) (PDB ID: 5B52) (54). Lower panel is the MvaT protomer structural homology model (see M&M). The color code is as in (A). (**C**) The electrostatic potential surfaces of H-NS and MvaT are depicted on full-length protomer structural models of the proteins using a red/white/blue color gradient. The negative and positive patches on the proteins' surfaces are indicated. In the lower panel is the five amino acid averaged charge window of the proteins protomers primary sequences. Positive, negative and neutral charged amino acid fragments are shown in blue, red and white bars, respectively. (**D**) Primary sequence alignment of selected members of the H-NS family of proteins from different bacterial organisms. The conserved positions of the charged amino acids in the protein's primary sequences are highlighted in blue (positive residues) in red (negative residues). The fold diagram of the H-NS monomer from *E. coli* is represented using the same color code in (A). The nomenclature of the N-terminal helices is indicated in black for the long H-NS family members and in magenta for the short members.

were harvested by centrifugation and the pellet was resuspended in the lysis buffer (20 mM Tris, 150 mM NaCl, 10 mM EDTA, pH 7). The cells were lysed using pre-cooled French press, and the lysate was centrifuged for 20 min at 8000 rpm. Next, the supernatant was loaded on a Heparin column (from GE healthcare Life sciences) and the protein was eluted by applying a NaCl gradient from 0.15 to 1 M. The eluted fractions were checked by SDS-PAGE and the ones that contain the MvaT dimer were pooled, concentrated and buffer changed using a PD10 column to 20 mM Bis–Tris, 50 mM KCl, pH 6. Next, the protein was loaded on a SP column (from GE healthcare Life sciences) and eluted by applying a NaCl gradient (from 0.15 to 1 M). The eluted fractions were also checked by SDS-PAGE and the ones that contain the MvaT dimer were pooled and concentrated to a 500 μL volume with an Amicon 10 kDa cut-off filter. The concentrated protein fractions were loaded on a GE Superdex 75 10/300 GL column and eluted with 20 mM Bis–Tris, 150 mM KCl, pH 6. The collected fractions were buffer exchanged to either 20 mM Bis–Tris, 50 mM KCl or 300 mM KCl, 1mM EDTA, pH 6. The purity of the protein was checked by SDS-PAGE (>95%) and the concentration was determined using a bicinchoninic acid assay.

The same procedure was used for the DBD overexpression and purification. The only difference in purification was in the first step where a nickel column was used instead of a heparin column.

### The tethered particle motion (TPM)

The Tethered Particle Motion experiments were done as previously described (20,41) and the flow cells were prepared with minor modifications. In short, first, the flow cell was washed with 100 μL of wash buffer (10 mM Tris–HCl pH 8, 150 mM NaCl, 1 mM EDTA, 1 mM DTT, 3% Glycerol, 100 μg/ml BSA (ac)) and experimental buffer (10 mM Tris pH 8, 10 mM EDTA, 5% glycerol with different salt concentrations as indicated in the text). The flow cell was sealed after adding protein (0 nM to 1600 nM) in experimental buffer, followed by 15 minutes of incubation. The measurements were initiated 15 min after introducing protein. For each flow cell more than 200 beads were measured at a temperature of 25°C. Data analysis was done as reported previously (20,41).

### Pull down bridging assay

The DNA Bridging Assay was performed as described previously (20,42), with minor modifications. The Streptavidin-coated Magnetic Dynabeads M280 (3 μL per sample) were resuspended in 6 μL coupling buffer (CB: 20 mM Tris–HCl pH 8.0, 2 mM EDTA, 2 M NaCl, 2 mg/ml BSA (ac), 0.04% Tween20) containing 3 μL of 100 fmol biotinylated 32% GC DNA (685 bp), and the bead suspensions were incubated for 20 min at 25°C on a shaker (1000 rpm). The beads were then washed twice with incubation buffer (IB: 10 mM Tris–HCl pH 8.0, 5% v/v glycerol, 1 mM spermidine) before resuspension in IB. Next, salt (KCl, NaCl, Kglu, $CaCl_2$, $MgCl_2$ or $MgSO_4$) was added to the desired concentration in each sample. Radioactive DNA (∼8000 cpm) was added to each sample and unlabeled 685 bp (32% GC) DNA was added to maintain a constant (2 fmol/μL) DNA concentration. MvaT or H-NS proteins were added to initiate the formation of bridged DNA–DNA complex. The mixture was incubated for 20 min (unless indicated otherwise) on the shaker at 1000 rpm at 25°C. After the incubation, the beads of each sample were washed once with its experimental buffer, before resuspension in 12 μL counting buffer (10 mM Tris pH 8.0, 1 mM EDTA, 200 mM NaCl, 0.2% SDS). The radioactive signal of samples was quantified by liquid scintillation over 5 min. Sample values recovered from the bridging assay were corrected for background signal (from a control sample without protein). The DNA recovery was calculated based on a reference sample containing the amount of labeled $^{32}P$ 685 bp DNA used in each sample and expressed as 'DNA recovery (%)'. All DNA bridging experiments were performed at least in duplicate. Each experiment contained 20 mM KCl, to which additional salt (KCl, NaCl, Kglu, $CaCl_2$, $MgCl_2$ or $MgSO_4$) was added depending on the tested experimental conditions.

### Electrophoretic mobility shift assay

The assay was performed on an AT-rich 200 bp DNA substrate (32%GC). Typically, 25 ng of DNA was incubated with different concentrations of the MvaT wild type or the MvaT dimer F36D/M44D in the binding buffer (10 mM Tris–HCl, 50 mM KCl, pH 7.5). The mixture was loaded on a 1% agarose gel (containing $1:10^4$ dilution of Gel red DNA stain) with 1 μL of 6× loading buffer (10 mM Tris–HCl pH 7.6, 0.03% bromophenol blue, 0.03% xylene cyanol FF, 60% glycerol and 60 mM EDTA). The samples were run at 16 mA for 4 h at 4°C in TAE standard buffer. The gels were visualized with a Bio-rad Gel Doc XR+ system.

### Circular dichroism

The MvaT wild type and F36D/M44D dimer far-UV CD spectra were recorded on a Jasco 810 CD spectrometer using a 10 μM protein solution in 20 mM Bis–Tris Buffer, 150 mM KCl, pH 6. The spectra were recorded in a 0.1 cm path length quartz cuvette using four scans with a bandwidth and a wavelength step of 1 nm. The obtained spectra were background corrected and smoothed using Jasco Spectra Manager.

### Isothermal titration calorimetry

ITC experiments were performed using a MicroCal VP-ITC system at 20°C. The samples contained 20 mM Bis–Tris, pH 6 with 50 mM KCl. Typically, 10 μM of MvaT F36D/M44D was placed in the cell (1.4 mL) and titrated with 360 μM (500 μL volume) of the DNA duplex d(CGCATATATGCG), injected in 2 μL aliquots. The delay time between the injections was 60 s with a stirring speed of 307 rpm. The corresponding 'protein to buffer' controls were performed for background correction. The ITC titration data were analysed using Origin 7.0 (OriginLab) provided with the instrument. Standard deviation was calculated from the fit by Origin.

### Small angle X-ray scattering

All the experiments were performed at the ESRF BioSAXS beamline BM29, Grenoble, France (43). Given the sensitivity of the batch SAXS mode for even small amounts of large soluble aggregates we used SEC-SAXS approaches to measure SAXS data only on monodisperse samples. A volume of 250 μL of protein for each MvaT sample was loaded on a GE Superdex 75 10/300 GL column *via* a high performance liquid chromatography (HPLC) system (DGU-20A5R, Shimadzu, France) attached directly to the sample-inlet valve of the BM29 sample changer. Low salt MvaT sample was measured at 11 mg/mL in 20 mM Bis–Tris, 50 mM KCl, pH 6.0, while high salt MvaT sample was measured at 9.5 mg/mL in 20 mM Bis–Tris, 300 mM KCl, pH 6.0. The column was equilibrated with three column volumes to obtain a stable background signal, which was confirmed before measurement. All the SAXS data were collected at a wavelength of 0.99 Å using a sample-to-detector (PILATUS 1 M, DECTRIS) distance of 2.81 m. The scattering of pure water was used to calibrate the intensity to absolute units (44). Data reduction was performed automatically using the EDNA pipeline (45). Frames in regions of stable $R_g$ were selected and averaged using PRIMUS (46) to yield a single averaged frame corresponding to the scattering of individual SEC species. Analysis of the overall parameters was carried out by PRIMUS from ATSAS 2.8.4 package (47) and by ScÅtter 3.0 software. The pair distance distribution function, $P(r)$, and maximum diameter of the particle ($D_{max}$) were calculated in GNOM using indirect Fourier transform method (48). The information on data collection and derived structural parameters is summarized in Supplementary Table S1. The pair distance distribution functions were used to calculate *ab initio* models in P1 symmetry with DAMMIN; the models were averaged, aligned and compared using DAMAVER (47).

### NMR resonance assignments

Sequential assignment of the MvaT dimer at 20°C was performed using the triple resonances HNCACB, CBCAcoNH, HNCA, HNcoCA, HNCO and HNcaCO experiments on a $^{15}$N, $^{13}$C MvaT F36D/M44D NMR sample (0.5 mM in 20 mM Bis–Tris, 150 mM KCl, 1 mM EDTA, pH 6). The NMR spectra were recorded on a Bruker Avance III (HD) 600 MHz spectrometer, equipped with TCI cryoprobe, processed by TopSpin 3.5 (Bruker Biospin) and analysed with Sparky software (49). The peak list of MvaT dimer was used to assign the MvaT dimer K31C mutant HSQC spectrum. The assignments of the MvaT F36D/M44D spectra are available from BMRB under entry 28010.

### NMR titration experiments

The NMR titration of the MvaT dimer and DBD with the 12 bp DNA substrate was performed on 95 and 100 μM $^{15}$N isotopically labelled protein samples, respectively, in 20 mM Bis–Tris buffer, 50 mM KCl or 300 mM KCl, pH 6 and 6% $D_2O$. A series of $^{1}$H–$^{15}$N HSQC spectra were acquired by gradually increasing the DNA:MvaT molar ratio from 0.1 or 0.2 to 1.6. The experiments were recorded at 20°C on a Bruker Avance III (HD) 600 MHz spectrometer, equipped with TCI cryoprobe, processed by TopSpin 3.5 (Bruker Biospin) and analysed by CCPnmr software (50). The MvaT dimer titration with KCl was conducted using the same procedure. The reference titration points were collected in a solution with 20 mM Bis–Tris, 50 mM KCl, pH 6 and the potassium chloride concentration was increased in steps to 100, 150, 200, 250 and 300 mM KCl.

The changes in peak positions and intensities were analysed by an in-house python script and the average chemical shift perturbations (CSP) were calculated using equation (1):

$$\Delta\delta_{avg} = \sqrt{\Delta\delta_H{}^2 + \frac{\Delta\delta_N{}^2}{6.25^2}} \quad (1)$$

Line shape analysis of the titration data was performed by TITAN (51) using a two-state binding model.

### Protein labeling and PRE measurement

To attach the MTS [(1-acetyl-2,2,5,5-tetramethyl-3-pyrroline-3-methyl)-methanethiosulfonate] and MTSL [*S*-(1-oxyl-2,2,5,5-tetramethyl-2,5-dihydro-1H-pyrrol-3-yl)methyl methanesulfonothioate] spin labels (bio-connect Life sciences) on the MvaT dimer surface, K31 was substituted with a cysteine. A $^{15}$N isotopically labelled sample of the variant MvaT K31C/F36D/K44D was produced using the procedure described above. The purified protein was first incubated for 1 hour at room temperature in the presence of 10 mM DTT to reduce disulphide bonds, followed by buffer exchange using PD10 desalting column. The protein was directly eluted into a solution of 20 times molar excess of MTS or MTSL. The mixture was incubated for 1 h stirring at 4°C. The sample was concentrated to a volume of 500 μL with an Amicon 10 kDa cut-off filter and injected into a GE Superdex 75 10/300 GL column to remove excess spin label. Incorporation of MTSL was >95% according to mass spectrometry, and the dimeric state of the conjugated protein was checked by analytical size exclusion chromatography. PREs were obtained using $^{1}$H–$^{15}$N TROSY spectra of 185 μM MvaT in 20 mM Tris, pH 6 at low salt (50 mM KCl) or high salt (300 mM) and in the presence or absence of DNA, with a DNA-to-protein molar ratio of 1.6. The TROSY spectra of the diamagnetic and paramagnetic samples were processed using TopSpin 3.5 and peak intensities and line widths were extracted using CCPnmr analysis (50). The paramagnetic contribution to the transverse relaxation rate (R2sp) was estimated from the measured intensity ratio of the paramagnetic and diamagnetic samples using equation (52) (2):

$$I_{para}/I_{dia} = \frac{R_2 \exp(-R_2sp * t)}{(R_2 + R_{2sp})} \quad (2)$$

where $I_{para}/I_{dia}$ is the measured intensity ratio, $R_2$ is the relaxation rate estimated from the widths at the half-height of the diamagnetic sample resonances, and $t$ is the time during which $^{1}$H magnetization is in the transverse plane during the TROSY pulse sequence (10 ms).

### MvaT structure homology modeling

The full-length MvaT dimer was constructed by combining a homology model of the dimerization domain (residues 1–78) and the NMR structure of the DNA binding domain (PDB ID: 2MXE) (53) (residues 79–124), using Modeller version 9.15. The homology model for the dimerization domain was obtained by aligning residues 1–78 of MvaT to the crystal structure of the N-terminal domain of *P. putida* TurB (PDB ID: 5B52) (54).

### Conjoint ensemble refinement against PRE and SAXS data

All simulations were performed in Xplor-NIH (55,56), starting from the homology model of the MvaT F36D/M44D dimer generated in this work (see text). The positions of the N-terminal domains of the MvaT dimer (residues 1–47) were fixed, the C-terminal DNA-binding domain (residues 83–122) was treated as a rigid-body group, while the intervening linker was given full degree of freedom. The computational protocol comprised an initial rigid-body simulated annealing step followed by the side-chain energy minimization as described before (57). The energy function consisted of standard geometric (bonds, angles, dihedrals and impropers) and steric (van der Waals) terms, a knowledge-based dihedral angle potential, and the PRE and SAXS energy terms incorporating the experimental data (58). Truncated SAXS curves ($q < 0.4$ Å$^{-1}$) and the PRE data for the C-terminal DNA-binding domain and the interdomain linker (residues 50–124) at each salt condition were used as the experimental input (57,58). Multiple copies of MvaT dimers ($N = 1$–5) were refined simultaneously in order to simulate molecular ensembles of multiple conformers (57) (Note that this procedure allows for the atomic overlap among MvaT molecules constituting an ensemble). In each run, 100 independent calculations were performed, and 10 lowest-energy solutions were selected for further analysis.

During the simulations, the PRE contributions from both subunits were taken into account. The PRE for each residue was defined as the sum of four contributions: (i) PRE from spin label (SL) on subunit 1 to the residue on subunit 1; (ii) PRE from SL on subunit 1 to the residue on subunit 2; (iii) PRE from SL on subunit 2 to the residue on subunit 2; (iv) PRE from SL on subunit 2 to the residue on subunit 1.

To assess the agreement between the observed PREs and the PREs back-calculated from the simulated ensembles generated in each run, we calculated the $Q$ factor (59), equation (3):

$$Q = \sqrt{\sum_i \left(\Gamma_{2,i}^{\mathrm{obs}} - \Gamma_{2,i}^{\mathrm{calc}}\right)^2 / \sum_i \left(\Gamma_{2,i}^{\mathrm{obs}}\right)^2} \qquad (3)$$

where $\Gamma_{2,i}^{\mathrm{calc}}$ is given by equation (4):

$$\Gamma_{2,i}^{\mathrm{calc}} = \frac{1}{N} \sum_{j=1}^{N} \Gamma_{2,ij} \qquad (4)$$

where $N$ is the ensemble size and $\Gamma_{2,ij}$ is the PRE back-calculated for the amide proton of residue ($i$) of the ensemble member ($j$).

The agreement with the experimental SAXS data in each run was assessed by calculating $\chi^2$ with the calcSAXS helper program (57), which is part of the Xplor-NIH v 2.49 package used in this work, assuming equal conformer populations in the simulated ensembles. The lowest energy structures of the MvaT dimer obtained from the ensemble modeling were fitted into the *ab initio* molecular shapes obtained by DAMMIN using UCSF Chimera software (60). The MvaT structural ensembles are submitted to SASDB with accession codes: SASDGS5 for MvaT (low salt) and SASDGT5 for MvaT (high salt).

## RESULTS

### Fold topology and electrostatics of H-NS family proteins

Primary sequence alignments and secondary structure predictions of twelve members of the H-NS family of proteins, from different bacteria, reveal a conserved fold topology (Supplementary Figure S1). Their C-terminal DBD contains, in most cases, two β-strands and two α-helices. The domain is connected to an N-terminal domain via a disordered linker. The N-terminal domain contains α-helices connected via random coils, but the number of helices may differ. Based on these criteria, two classes of H-NS members could be distinguished: long and short versions of H-NS. The long H-NS members have an N-terminal domain which includes four helices (α1, α2, α3 and α4), forming a dimerization site (site 1) between the H-NS monomers and an oligomerization site (site 2) between its protomers (Figure 1A). The crystal structure of the H-NS N-terminal domain (1–83) has shown that site 1 is formed by a 'handshake fold' topology between α1 and α2 and part of α3. Site 1 is stabilized by a hydrophobic core and salt bridges (31,32) (Figure 1A). In the short members (MvaT; MvaU; TurA and TurB), these two N-terminal helices are missing (Figure 1B; Supplementary Figure S1). The crystal structure of the TurB N-terminal domain (1- 61) has revealed that site 1 is formed by a 'coiled-coil motif' between the N-terminal helices α1 (corresponding to H-NS α3) of two monomers (54) (Figure 1B).

Using the TurB N-terminal domain crystal structure, we have built a homology model of the MvaT dimerization site which was connected via the flexible linkers to the NMR structure of the protein DNA binding domains (PDB ID: 2MXE) (53), thus obtaining a full-length structural model of the MvaT protomer (Figure 1B). We used this model for structural investigation.

In contrast to the differences in site 1, the oligomerization site (site 2) fold architecture appears to be conserved between these members of the H-NS family (Figure 1A, B). This site is also formed by hydrophobic interactions between two α-helices (α4 and α2 for the long and short members, respectively) and stabilized by salt bridges (32,54).

One striking characteristic is a local degree of conservation of the electrostatic potential between H-NS and MvaT protomers. Their electrostatic potential surfaces show that the N-terminal domain (helices α3 and α1 of H-NS and MvaT, respectively) contain negatively charged surface patches, whereas the C-terminal domain and the linker region contain positively charged regions (Figure 1C).

This characteristic appears to be shared between the H-NS family members, as it can be predicted from the conserved position of the negatively and positively charged residues within their primary sequences (Figure 1D). The five amino acid averaged charge window analysis of the primary sequences revealed that the α-helices in the N-terminal domain include predominantly negatively charged regions, while the linkers and the DNA binding domains are mostly positively charged, as they both contribute to DNA binding (61–63) (Figure 1D; Supplementary Figure S1). Additionally, α1 and α2 of the long H-NS members are positively charged in line with their contribution to the interaction with DNA (31) (Figure 1D; Supplementary Figure S1). Thus, this asymmetrical charge distribution seems to be a conserved feature between H-NS family members suggesting a specific role in their function.

In solution, it is expected that the two DNA binding domains of the H-NS protomers behave as 'beads on a flexible string', where the function of the linkers is to enable a relatively unhindered spatial search by the attached domains. Thus, electrostatic interactions between the oppositely charged domains, as suggested by earlier studies (20,25), might occur. These interactions are potentially sensitive to changes of ionic strengths in the protein environment.

### Salt induces global conformational changes in MvaT protomer

To test our hypothesis that the MvaT protomer conformation is sensitive to changes in ionic strength of the surrounding medium, we employed a combination of circular dichroism, small-angle X-ray scattering (SAXS) and NMR spectroscopy. To this purpose, we engineered an MvaT variant in which oligomerization was abolished by substituting site 2 residues F36 and M44 with aspartic acid (D), remote from the negative charge patch of the N-terminal region. As site 1 is left unchanged, it was expected that MvaT could still form dimers, which was confirmed by size-exclusion chromatography (Supplementary Figure S2A, B). The double mutation induces changes in the MvaT α-helical content as concluded from the overlay between the wild type and the mutant far UV CD spectra (Supplementary Figure S2C). A similar observation was reported for H-NS from *S. typhimurium*, which was attributed to the loss of the protein oligomerization ability (33). In the oligomeric state the helix of site 2 (α2) is locked in a helical structure by interacting with its counterpart from another MvaT dimer. In the dimeric state this helix seems to experience exchange between extended and helical conformations (Figure 2D).

The effect of the double mutation on the binding of MvaT to DNA was assessed by electrophoretic mobility shift assay (Supplementary Figure S2D, E). Binding of the MvaT wild type caused a major reduction in DNA substrate mobility, whereas for the double mutant DNA mobility was only mildly affected. We attribute this to a lack of DNA binding cooperativity for the dimeric MvaT derivative, as confirmed by tethered particle motion (see Materials and Methods) (Supplementary Figure S2F).

SAXS was employed to assess the effect of salt concentration on the global conformation of the MvaT F36D/M44D dimer (Figure 2A and Supplementary Table S1). Under low salt conditions (50 mM KCl) the MvaT protomer adopts a relatively compact conformation as evidenced by the normalised Kratky plot and the particle's Porod exponent (3.2) (Supplementary Table S1). Interestingly, at high salt concentrations (300 mM KCl), the MvaT protomer displays an increased flexibility, which is reflected by an increase in $R_g$ (3.56 nm versus 3.83 nm) and $D_{max}$ (14.70 nm versus 15.84 nm), a decrease in Porod exponent (3.2 versus 2.7), and the appearance of the normalised Kratky plot (Figure 2A and Supplementary Table S1).

In parallel to the SAXS analysis, we produced an isotopically labelled $^{15}N$,$^{13}C$ MvaT sample for which the $^{1}H$–$^{15}N$ HSQC NMR spectrum was assigned at 150 mM KCl. The protein spectrum shows well-dispersed resonances corresponding to residues of the DBD and multiple overlapped peaks (crowded region) centred ∼8.2 ppm in the $^{1}H$ dimension, reporting on the helical N-terminal domain and the disordered linker (Figure 2B). Remarkably, the MvaT spectrum shows more resonances than expected, indicating the presence of two forms. Two resonances are observed for the amide groups of residues 45–47 and residue 53, which form the oligomerization site (site 2), and of residues 61–65 in the linker region (Figure 2B). Amides of the 'coiled-coil' (site 1) show weak resonances and several of them could not be assigned due to broad lines (Figure 2B). The Cα and Cβ chemical shifts were used to predict the secondary structure probability of the MvaT dimer in solution (Figure 2D). Amino acid sequences of α-helix 2 (51–58), the linker (60–80) and of short stretches of α1 appear to be disordered. The presence of intrinsically disordered regions agrees with the secondary structure prediction from the far-UV CD spectrum. The deconvolution of the protein CD spectrum revealed that 40–45% of the protein is disordered (Figure 2C).

Next, we investigated the binding of potassium chloride to the MvaT protomer by NMR titration. Small chemical shift perturbations (CSP) in the fast exchange regime were observed for multiple resonances. Residues exhibiting CSP are scattered on regions of site 1, site 2, the linker and the DBD in the structural model of the MvaT dimer (Figure 2F), suggesting a non-specific effect due to the increase in ionic strength. Interestingly, the protein resonances show a general yet non-uniform increase of intensities at high salt compared to low salt. This suggests a decrease in the rotational correlation time of the protein folded domains (Figure 2G), possibly caused by the disruption of their intramolecular interactions. This observation is in line with the larger radius of gyration and the enhancement of protein flexibility derived from the SAXS data.

In conclusion, the increase in ionic strength, indeed induces global conformational changes of the MvaT dimer by shifting its conformational equilibrium from relatively compact to extended and flexible states. These structural changes are possibly due to the salt modulation of the postulated intramolecular electrostatic interactions between the oppositely charged regions of the MvaT protomer.

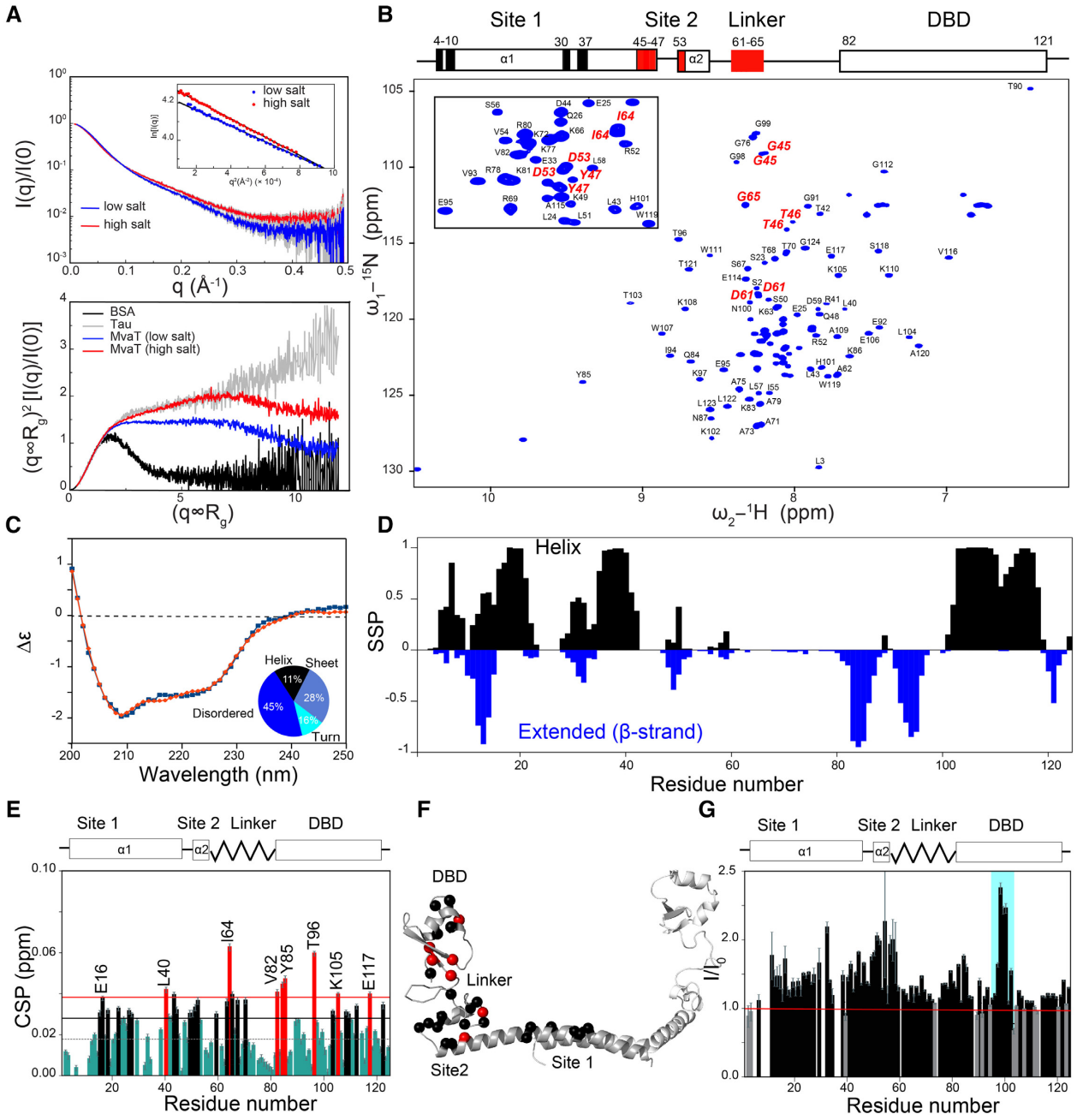


**Figure 2.** Global conformational changes in MvaT induced by salt. (**A**) SAXS experiments. The top panel displays the SAXS data obtained for the MvaT dimer under low salt (50 mM KCl) and high salt (300 mM KCl) conditions indicated by the blue and red curves, respectively. The error margins are colored in gray. The inset shows the Guinier regions of both data sets. The bottom panel displays the normalised Kratky plots for the MvaT dimer under both salt conditions. An intrinsically disordered standard (Tau, gray trace) and a rigid, globular standard (BSA, black trace) are shown for comparison. (**B**) Assignment of the $^{1}H$–$^{15}N$ HSQC MvaT spectrum (at 150 mM KCl). Residues that appear as double peaks in the spectrum are labelled in red. Insert is a zoom in at the crowded region of the spectrum. The layout of the MvaT domains is shown above the spectrum. Residue positions with non-observable resonances in the HSQC spectrum are marked by black rectangles. The residue positions with two observable resonances are in red. (**C**) Circular dichroism spectra of MvaT dimer (experimental data in blue and spectrum deconvoluted using BeStSel in red (64)). (**D**) Secondary structure probability (SSP) plot of the MvaT dimer derived from Cα and Cβ chemical shifts, determined by PECAN (65). Negative values in blue bars indicate β-strand or extended secondary structures and positive values in black bars indicate α-helices. (**E**) Weighted average CSP of the MvaT resonances between 50 and 300 mM KCl. Resonances with CSP more than two (red line) or one (black line) standard deviation (SD) from the 10% trimmed mean (gray dashed line) are labelled and shown in red, black and green bars, respectively. (**F**) Residues exhibiting CSP mapped on the structural model of the MvaT dimer (see Materials and Methods). Amide nitrogens with a CSP > 1 and 2 SD trimmed mean are shown in spheres and colored in black and red, respectively. (**G**) The HSQC peak intensity ratio of the MvaT dimer at 300 mM KCl (I) and 50 mM KCl ($I_0$). Gray bars indicate residues with minor peak intensity changes between the two salt conditions. Loop 95–102 of the DBD is highlighted with a cyan rectangle.

### Salt modulation of the MvaT dimer conformational landscape

To obtain more information about the conformational changes induced by salt on the MvaT dimer, we used paramagnetic relaxation enhancement (PRE) NMR spectroscopy. PRE reports on long-range structural distances (20–30 Å) between a paramagnetic spin label and the amide protons of the protein (66). Amide protons on residues within 30 Å from the spin label experience an increase in relaxation rate resulting in broadening of their NMR resonances and intensity reduction. To measure PRE on the MvaT dimer, we substituted residue K31 with a cysteine and conjugated it with either a paramagnetic (MTSL) or a diamagnetic (MTS) probe (see Materials and Methods).

Under low salt condition (50 mM KCl), strong PRE effects were observed for residues of site 1 (1–48) (Figure 3A). These residues were excluded from the analysis as they display weak peak intensities in the HSQC diamagnetic spectrum and sense the paramagnetic effects from spin labels on both MvaT subunits. Residues of site 2 (49–60) and the linker region (61–80) exhibit also strong PREs, indicating that the amide nuclei spend at least part of the time close the probe (Figure 3A). A weak PRE effect occurred for residues of the DBD, except for the loop between 95 and 105 that, in the DNA-bound state, is known to intercalate with the DNA minor groove (53). The strong PRE effects within this loop suggest a rather localized interaction between the DBD and a region of the protein close to the spin label.

At 300 mM KCl, the PRE pattern is overall similar, but a decrease in PRE is observed for the site 2 residues, the linker regions and loop 95–105 of the DBD (Figure 3B). Under this condition, these regions could either be populating conformations in which the nuclei are further away from the spin label or spend a smaller fraction of the time in the conformation close to the spin label.

To investigate the structural states sampled by the MvaT dimer under both salt conditions, we performed ensemble calculation using an Xplor-NIH protocol which combines the PRE and SAXS data as structural restraints. For each condition, we simulated molecular ensembles of multiple conformers ($N = 1$–5) and assessed their agreement with the experimental data by calculating the corresponding quality metrics (PRE Q-factor and the SAXS $\chi^2$) (see Materials and Methods). The best solutions for the low salt were obtained with $N = 3$ ($Q = 0.21$; $\chi^2 = 1.43$) (Figure 3C; Supplementary Figure S3A) and for the high salt with $N = 2$ ($Q = 0.37$; $\chi^2 = 1.33$) (Figure 3D; Supplementary Figure S3B). The 10 lowest-energy solutions for each ensemble fit well within the molecular shapes determined by DAMMIF (Figure 3E, F) (67).

In agreement with the flexibility observed for MvaT in both low and high salt conditions (with a significantly more pronounced flexibility at high salt concentration), the SAXS and PRE data sets could only be described by a conformational ensemble. As expected, under low-salt conditions the MvaT ensemble is composed of rather compact conformers, while at higher salt concentrations the ensemble members adopt more extended conformations due to an increased flexibility (Figure 3E, F).

Based on the DBD position relative to the N-terminal domain two major species could be distinguished in both conformational ensembles: half-opened and fully-opened forms. In the half-opened states, the DBD is bound to the N-terminal domain, while the other domain is free (Figure 3G, H). The occupancy of the N-terminal domain with one of the DBD of the dimer appears to prevent simultaneous binding of the second DBD to the N-terminal domain due to steric hinderance. This might explain the observed asymmetrical structural configuration of the MvaT homodimer in the half-open forms.

In the fully-opened states, both DBDs are not bound to the N-terminal domain but can still be close to each other in space. Both of conformational species comprise several subpopulations with different radii of gyration (Figure 3E, F).

Under both salt conditions, the DBD in the major conformer of the half-opened states exhibits similar intrasubunit binding modes to the N-terminal domain, although a slight difference in orientation is observed (Supplementary Figure S3C). The binding interface includes the positively charged loop 95-ET**K**GGN**HK**-102 (charge = 1.8, pH 6) of the DBD and the negatively charged segment 26-Q**DD**KLKK**EL**E**DEE**-38 (charge = –3.8, pH 6) of the N-terminal domain. In contrast, at low salt the linker appears to form closer interactions with the negatively charged patch of the N-terminal domain (26–38) compared to the high salt condition. This indicates that the linker might be involved in stabilizing the DBD–N-terminal domain complex.

In conclusion, the structural study reveals the existence of electrostatic interdomain interactions between the DBD and N-terminal domains of MvaT which are further stabilized by the linker region. Increase in salt concentration induces delicate changes within the MvaT protomer conformational landscape by weakening these intramolecular interactions and increasing the exchange rate between the half-open and open conformers. Consequently, the protein samples a larger conformational space.

### The DNA substrate contributes to the MvaT protomer conformational opening

Owing to the negative charge and specificity for the DBD it is conceivable that the DNA also modulates the interdomain interactions of the MvaT protomer. To test this hypothesis, a titration of the MvaT dimer with a 12 bp AT-rich DNA substrate at low (50 mM KCl) and high salt (300 mM KCl) concentrations, was performed using NMR. At low salt, significant CSP were observed for residues of the DBD. At the DNA:MvaT molar ratio of 1.6, a general line broadening of the DBD peaks is observed attributed to the increase of its rotational correlation time ($\tau_c$) upon complex formation, independent of the protomer N-terminal domain (Supplementary Figure S4A). Analysis of the titration data using a 1:1 binding model yields a $K_D = 44 \pm 5$ nM and $k_{off} = 280 \pm 5$ s$^{-1}$ (Supplementary Figure S4C). The affinity is too high to be deduced from this NMR titration with accuracy. Therefore, we used ITC for validation, yielding $K_D = 30 \pm 2$ nM (Supplementary Figure S4D). No significant CSP for the N-terminal domain residues were ob-

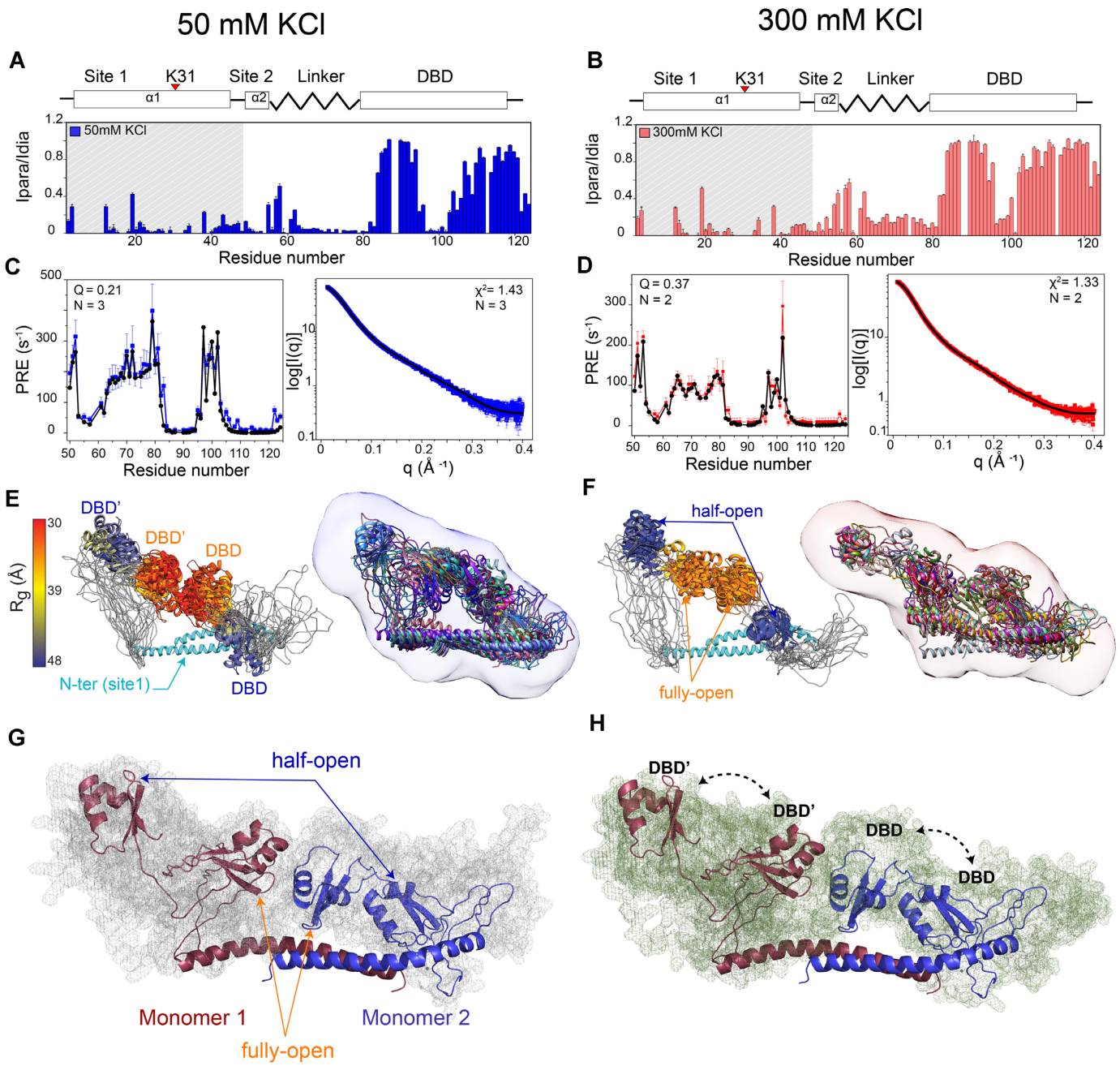


**Figure 3.** MvaT dimer structural ensembles at low and high salt conditions. (**A**, **B**) The PRE-intensity ratio (Ipara/Idia) vs. residues number of the MvaT dimer at 50 mM KCl (blue bars) and 300 mM KCl (red bars), respectively. PRE from residues in the shaded region were excluded from the analysis. The structure of the MvaT monomer is shown schematically above the panels and the MTSL labeling position is indicated by the red triangle. The error bars are inversely proportional to the propagated signal-to-noise ratio of individual resonances. (**C** and **D**) The experimental PRE and SAXS curves (50 mM KCl in blue and 300 mM KCl in red) fit (black line) to the top conformers of the low and high salt ensembles, respectively. (**E**, **F**) Low (E) and high salt (F) best conformers colored by their radius of gyration using a blue/orange gradient, respectively. The color gradient is depicted only on the DBD of the MvaT dimer (DBD' and DBD refer to MvaT subunits 1 and 2, respectively). The best conformers are fitted into the *ab initio* molecular shapes generated by DAMMIF (67). The low (**G**) and high salt (**H**) half-open and fully open conformers of the MvaT dimer, classified based on the position of DBDs relative to the N-terminal domain. The atomic probability distribution maps of the low and high salt ensembles are shown in gray and green meshes, respectively. The MvaT monomers are colored in red and blue. The dashed arrows indicate the exchange between the DBD configurations.

served, indicating that the interactions with the short DNA substrate are limited to the DBD and a few residues of the linker region (Figure 4A). However, a 1:1 binding model may be an oversimplification.

The ensemble structure of the MvaT dimer at 50 mM KCl revealed that interactions between the DBD and the N-terminal domain occur, with only one of the two DBD binding at any time, effectively creating two populations of DBD (Figure 4D). Thus, one DBD is free to bind to the DNA, whereas for the other competition for binding occurs between DNA and the N-terminal domain. The NMR spectra seem to catch this difference in the DBD forms at a DNA:MvaT molar ratio of 0.2, showing two peaks with different CSP for the DBD resonances (Figures 4C and 3E). In the absence of DNA, the DBD will be in exchange between bound and free states, and also within the bound state, it may sample multiple interactions in an encounter complex like state. Broad lines are observed for multiple amide resonances including the ones that correspond to residues of loop 95–105 (Supplementary Figure S3D; 2g), suggesting that these exchange processes are intermediate to fast on the NMR time scale (i.e. the chemical shift differences between bound and free). Addition of DNA will bind the population of free DBD preferably, splitting the resonances of the two populations, provided the exchange rate between the states of DBD bound to the N-terminal domain and bound to the DNA is sufficiently slow. At higher concentrations of DNA the exchange rate is increased ($k_{ex} = k_{on}$[DNA] + $k_{off}$) and the exchange between the two DBD populations is too fast to result in double peaks. This model is supported by titration studies of the isolated DBD with DNA. In the absence of the N-terminal domain, the resonances of the DBD show single peaks at 0.1 and 0.2 DNA:MvaT molar ratios (Supplementary Figure S3E).

At high salt, the interdomain interactions are weakened by the ionic strength and the exchange rates between the DBD free and bound to the N-terminal becomes fast on the NMR time scale. Therefore, the peak splitting, observed under the low salt condition, becomes invisible (Figure 4C, D). Interestingly, in this case smaller amplitudes of CSP are observed upon DNA binding, yet with the same direction as for the low salt (Figure 4B). This suggests that part of the complex is in an encounter state which is in equilibrium with the specific state and does not contribute to CSP (68). Nonetheless, a general line broadening of the DBD resonances remained observable (Supplementary Figure S4B) and residues involved in the direct interaction with the DNA disappear. Analysis of the titration data yields a $K_D = 7.7 \pm 0.3$ μM and a $k_{off} = 2 \pm 0.2 \times 10^3$ $s^{-1}$ (Supplementary Figure S4B,C).

The conformational opening of the MvaT protomer induced by DNA, at low and high salt, was probed by changes in the PRE upon addition of DNA (at DNA:MvaT = 1.6). At low salt, a substantial loss in the PRE is observed for residues 60–80 of the linker region and the dimerization site 2 (Figure 4E). Almost no PRE effect on the DBD was observed. This indicates that the protein is adopting a fully-opened conformation in which the DNA substrate is shielding the DBD and part of the linker region from the interaction with the N-terminal domain. At high salt, this effect is less pronounced, yet DNA still reduces the PRE (Figure 4F). These results provide evidence that salt and DNA substrate have an additive effect on the conformational opening of the MvaT protomer.

### Modulation of MvaT electrostatic interdomain interactions by salt and DNA drives the switch between its DNA binding modes

Our structural studies have established that the MvaT dimer samples a heterogenous conformational space dominated by half open and fully open conformers. Increase in salt and DNA concentrations destabilizes the electrostatic interactions between the DBD and the N-terminal domain. Consequently, the exchange rate between the half open and fully open conformers becomes fast and the sequestration of the DBD by the N-terminal domain is diminished. Thus, the protomers can potentially interact simultaneously with two independent DNA segments.

To test whether this dynamic conformational equilibrium has implications for the structure and function of MvaT wild type-DNA complexes, we determined the modes of DNA binding under the low and high salt conditions using tethered particle motion (TPM) and bridging pull-down assay (20,42).

First, we investigated the effect of salt on lateral nucleoprotein formation by oligomerization of MvaT along DNA. In TPM the length and stiffness of the tethered DNA molecules is correlated to the root mean square displacement (RMS) of the attached polystyrene bead. The formation of a filament along DNA results in DNA stiffening, observed as an increase in RMS by TPM. The RMS changes of the polystyrene bead attached to a single DNA molecule (685 bp, 32% GC) were determined as a function of protein concentration. The experiment was performed at 50 mM KCl (low salt) and 315 mM KCl (high salt) (Figure 5A). Under both conditions two binding regimes were evident. At low MvaT concentration, a decrease in RMS was observed, which is attributed to the ability of MvaT to bend double stranded DNA (phase I) (53). We propose that this regime represents a nucleation phase where MvaT protomers bind non-cooperatively to the DNA substrate (Figure 5C). In the second regime (II), a gradual increase in RMS occurs, which reaches a maximum of 160 nm at 1.6 μM of MvaT. This represents a phase in which the MvaT protomers gradually oligomerize along the DNA until saturation. The difference between the two salt conditions is in the first regime in which the DNA is bent by individual dimers (I). At high salt, the extent of DNA compaction resulting from DNA bending by MvaT is reduced (Figure 5A). This could be due to an effect of the counterions ($Cl^-$) on the DNA binding affinity of MvaT (as seen with H-NS) (20). To minimize this potential counterion effect, we also performed the TPM experiment using potassium glutamate (Kglu) instead of KCl. Indeed, the differences in the MvaT titration curves obtained at low and high salt were much less pronounced than with KCl (Figure 5B).

These results suggest that the low and high salt conditions have no effect on the MvaT DNA stiffening activity. At high salt, the delicate conformational changes due to the increase in flexibility and in exchange rates between the half-open and fully open states of MvaT protomers have no in-

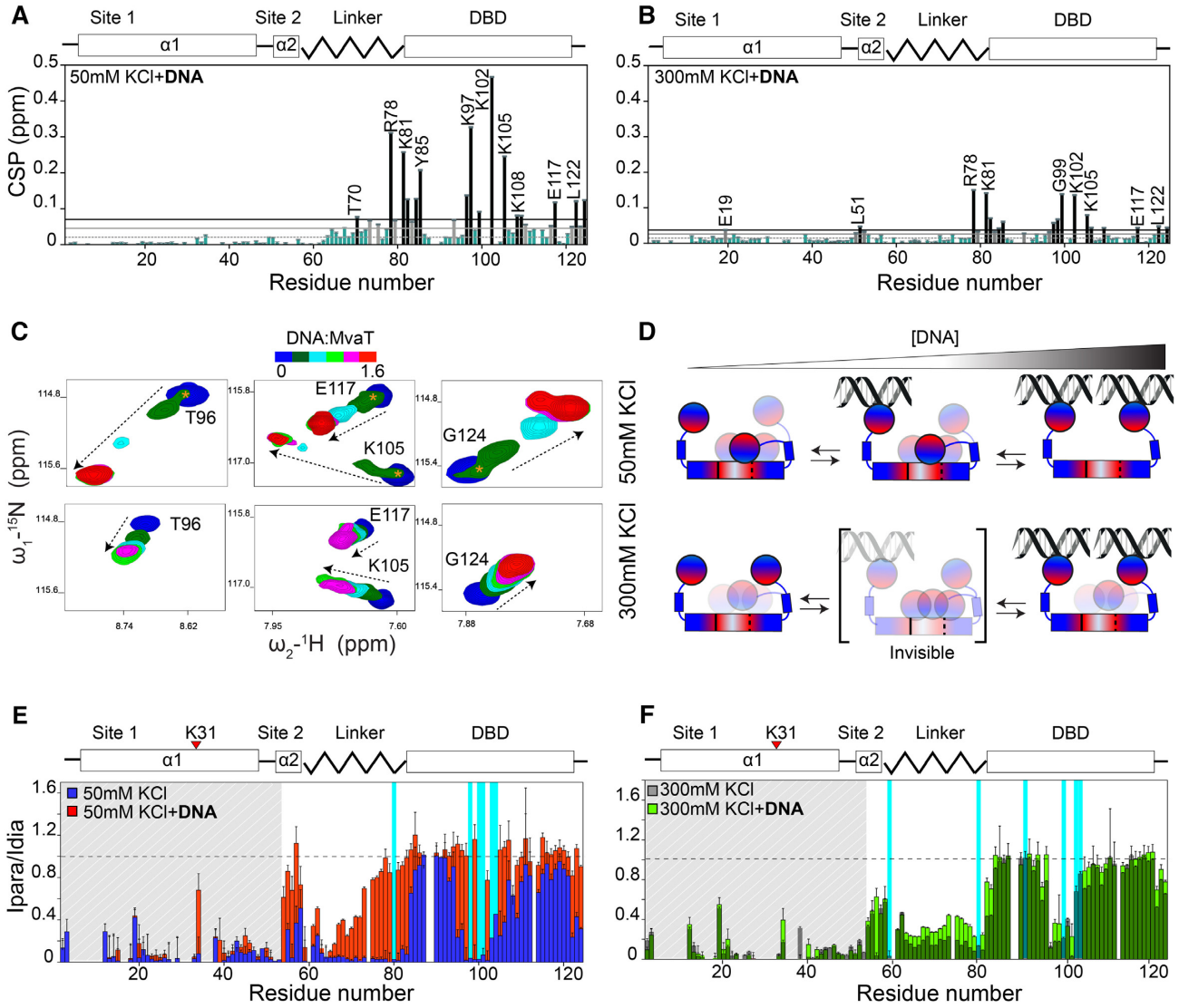


**Figure 4.** DNA modulates the conformational state of the MvaT dimer. (**A** and **B**) Analysis of the MvaT dimer HSQC spectra weighted average CSP at 1.6 DNA:MvaT molar ratio at 50 and 300 mM KCl, respectively. Resonances with CSP more than two (black line) or one (gray line) standard deviation (SD) from the 10% trimmed mean (gray dashed line) are labelled and shown in black, gray and green bars, respectively. (**C**) CSP amplitudes and directions (dashed arrows) of the DBD resonances upon titration with 12 bp DNA at 50 (upper panels) and 300 mM KCl (lower panels). The resonances that correspond to the N-terminal bound DBD are indicated by orange asterisks. (**D**) Schematic representation of the DNA binding mechanism to the MvaT dimer under low and high salt conditions. The electrostatic characteristics of the MvaT dimer are schematically shown by a red /white /blue color gradient. (**E** and **F**) Overlay between the PRE versus MvaT dimer residue number at low salt in the absence (blue bars) and presence of DNA (red bars) and high salt in absence (gray bars) and presence of DNA (green bars), respectively. Resonances with non-determined PRE, due to line broadening upon DNA binding, are highlighted in cyan bars. The layout of the MvaT monomer is shown in the upper panel. The position of the spin label is indicated by the red triangle.

fluence on this process. Besides, the dissociation effect of the increase in ionic strength on the complex is countered by the cooperative binding of the MvaT protomers along the DNA.

Previously we have demonstrated that H-NS switches between its DNA stiffening and bridging activities as function of $MgCl_2$ by using a sensitive and quantitative bridging pull-down assay (20). Here, we have used the same approach to test the effect of potassium chloride concentrations on MvaT-mediated DNA-DNA bridging. The DNA bridging efficiency (i.e. the percentage recovery of DNA from solution) as a function of KCl concentration (Figure 5D) revealed that at low salt concentration (50 mM KCl) the MvaT-mediated bridging activity is negligible despite the protein's ability to stiffen DNA by lateral nucleoprotein filament formation (Figure 5A). This agrees with our structural model in which MvaT protomers can bind to the DNA with only one of their DBDs while the other one is sequestered by the electrostatic interaction with the N-terminal domain. Under this condition, the lateral nucleoprotein filaments of MvaT cannot form a bridge between two DNA duplexes.

By increasing the salt concentration, an increase of the protein bridging efficiency is observed and reaches a maximum at 315 mM KCl (Phase I'). This dependency is also

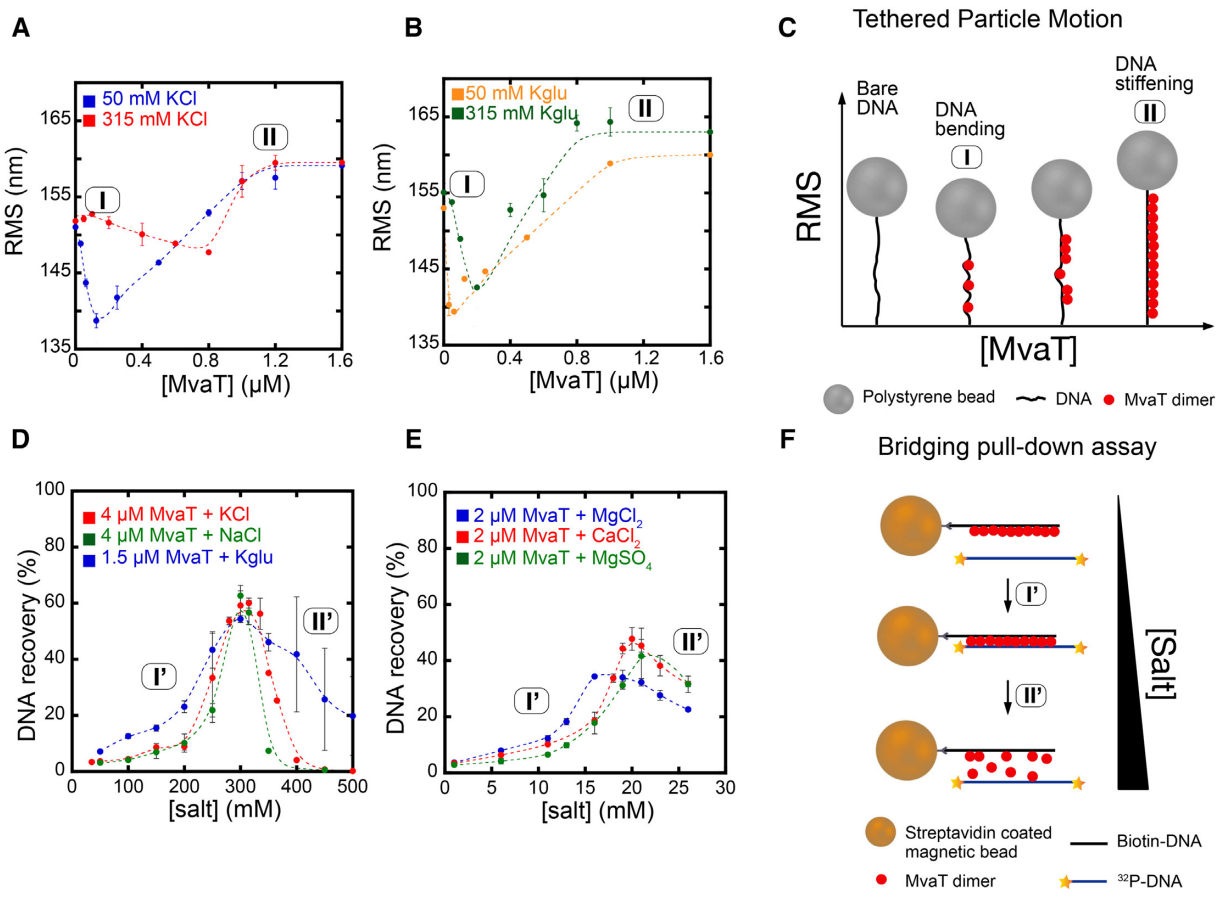


**Figure 5.** Conformational changes of MvaT induced by salt drive the switch between its DNA stiffening and bridging activities. (**A**) Root mean square displacement (RMS) of the tethered DNA particles as a function of MvaT concentration at 50 mM KCl (in blue) and 315 mM KCl (in red). The different regimes are labelled (I, II). (**B**) RMS as a function of MvaT concentration in the presence of 50 mM potassium glutamate (KGlu) (in yellow) and 315 m KGlu (in green). (**C**) Schematic representation of the experimental observations using the Tethered Particle Motion technique. The different regimes observed in (A) and (B) are labelled I and II. (**D**) DNA bridging efficiency of the MvaT wild type as a function of monovalent ions concentration: KCl (in red); NaCl (in green); KGlu (in blue). (**E**) The MvaT DNA bridging efficiency as a function of divalent ion concentration: $MgCl_2$ (in blue); $CaCl_2$ (in red) and $MgSO_4$ (in green). The different regimes of MvaT DNA bridging activity are labelled (I', II'). (**F**) Schematic representation of the experimental observations using the DNA bridging assay. The different regimes observed in (D) and (E) are labelled I' and II'. Error bars indicate ± SD of duplicate.

observed in the presence of Kglu and NaCl (Figure 5D, F). The low and high salt conditions have no effect on the protein oligomerization state (Supplementary Figure S5A).

We have also tested the effect of divalent ions on the MvaT DNA bridging activity using $MgCl_2$, $MgSO_4$ and $CaCl_2$: the DNA bridging efficiency of MvaT also depends on the tested divalent ions. However, optimum bridging efficiency is reached at lower salt concentrations (~18 mM for $MgCl_2$ and ~20 mM for $MgSO_4$ and $CaCl_2$) (Figure 5E).

Previously, the switch between DNA bridging and stiffening of H-NS family members was only observed and quantitatively analysed as a function of divalent ions (20,23). Here, we showed that the DNA bridging efficiency of MvaT also depends on monovalent ions, suggesting that the switch might not require specific ions. There are some indications that H-NS can also bridge DNA in the presence of 200 mM KCl and in absence of $MgCl_2$. While captured by AFM imaging, this observation was not corroborated by solution methods (24). To substantiate this observation, we here determined DNA bridging efficiency of H-NS in the presence of 50–200 mM KCl. Indeed, we observe a fourfold increase in the bridging efficiency between 50 and 100 mM KCl (Supplementary Figure S5c). These findings indicate that the switch between the DNA binding modes of H-NS proteins is independent from the type of ions and is mainly due to the increase in ionic strength. Note, however that divalent ions are more efficient (by 1 order of magnitude) in promoting bridging than monovalent ions. These differences are possibly due to the higher effective shielding of the protein's charged regions by multivalent ions.

The observed effect of ionic strength on the ability of MvaT to bridge DNA can be explained structurally. The increase in salt concentration gradually destabilizes the inter-domain electrostatic interactions of the MvaT protomers. DNA has an additive contribution on the shifting of the conformational equilibrium of the MvaT protomers towards the fully opened state. In this state, MvaT exposes most of the DNA binding domains in the lateral protein filament to concurrently interact with another DNA duplex and form a bridge. Beyond a certain threshold of ionic strength, the bridged protein–DNA complex starts disinte-

grating because the high ionic strength will weaken the interactions between the DNA binding domain of MvaT and DNA (Supplementary Figure S5b).

To corroborate this structure/function relationship mechanism in the context of MvaT nucleofilaments, amino acid residues located at the interface between the N-terminal and DBD domains were substituted to perturb formation of the interdomain complex. The ensemble structure calculation of the MvaT mutant dimer revealed that the interface between the two domains is formed by the negative region of the N-terminal domain (26-QDDKLKKELEDEE-38) and the positive loop of the DBD (95-ETKGGNHK-102). Substitution of E35/E37/E38 with alanine or E33/E37 with glutamine, yielded MvaT variants capable of oligomerization in solution (data not shown) and of bridging DNA duplexes at low (100 mM) and high (300 mM) salt concentrations (Supplementary Figure S6A, B). These MvaT variants are also able to bend and stiffen DNA, yet to a lesser extent when compared to the wild type protein (Supplementary Figure S6c).

These macroscopic observations provide direct evidence that the electrostatic interactions of the DBD and N-terminus of MvaT change, in response to altered ionic strength, which translates into altered DNA binding properties. Salt and DNA function additively to disrupt these interdomain interactions, thus inducing the required conformational changes that drive the switch between the DNA bridging and stiffening activities of the H-NS family of proteins.

## DISCUSSION

The mechanism by which H-NS family proteins sense the osmotic environment to modulate bacterial nucleoid organization and gene transcription is poorly understood. H-NS proteins form lateral nucleoprotein filaments along the DNA or bridge two DNA duplexes, resulting in DNA loops. Divalent ions drive the switch between DNA stiffening and bridging activities of the H-NS family members (17,20,23).

Our previous studies suggested that the switch between the two DNA binding modes requires H-NS protomers to experience conformational changes between an open and a closed state (20). Although the study was based on MD simulation and supported by mutagenesis, a detailed structural description of the protein conformational landscape based on experimental evidence was missing. To test this model, we have used MvaT from *P. aeruginosa*, which we argue represents a short structural version of H-NS as a benchmark.

Analysis of the primary sequences of H-NS family members has revealed conserved positions of charged residues despite the low sequence identity. A cluster of negatively charged residues is in the N-terminal domain whereas the DNA binding domain and the linker region contain positively charged residues. Thus, we hypothesized that electrostatic interactions between the two oppositely charges domains may take place, which could be modulated by the increase in ionic strength.

By combining PREs and SAXS techniques we have modeled the conformational landscape of the MvaT dimer under low and high salt conditions. Under both conditions, the protein samples heterogeneous conformational space where the two DNA binding domains adopt different spatial configurations. Two major conformers could be identified: a half-opened and a fully opened state. In the half-opened state, one of the DNA binding domains is interacting with the α2 N-terminal helix in an encounter complex like states. The interface between the two domains comprises the positively charged loop 95-ET**K**GGN**HK**-102 and the negatively charged segment 26-Q**DD**KLKK**E**L**EDEE**-38 of the DBD and the N-terminal α2, respectively. At low salt, these interactions prevent one of the DBDs of the MvaT protomer from forming a complex with DNA. At high salt, this electrostatic intramolecular complex is destabilized, causing an increase in exchange rate between the open and close states and thus a delicate change in the conformational space of the protein where it becomes more flexible and extended. This effect is enhanced by DNA substrate which induces the opening of the MvaT dimer by shielding the DBD from interacting with the N-terminal domain.

These findings agree with what has been proposed for H-NS. The MD simulations of the H-NS dimer in the presence of 50 mM KCl revealed interactions between its DBD and its N-terminal domain involving a negative amino acid patch in the α-helix 3 (E42–E50) and the positively charged regions 98–105 (KYSYVDENGE) and 123–129 (EQGKS) of the DBD (20). These interactions are altered in the presence of 130 mM KCl or 10 mM $MgCl_2$. Recently, Arold *et al.* confirmed these findings by NMR titration of the N-terminal domain (2–57) with the DNA binding domain (84–137). The interdomain interactions were lost at high salt concentration. However, the authors claim that the occurrence of these interactions within the protein nucleofilament is not possible due to stereochemical restraints (as the linker is 25–30 Å from site 1) unless the oligomerization site 2 unfolds (25). We disagree with these claims as the linker region and the DNA binding domain together have a length of >40 Å, which provides the DBD with enough space and degree of freedom to reach the negative residues in α-helix 3. Additionally, disruption of the H-NS interdomain interactions by mutagenesis has generated a variant that adopts an open conformational state and oligomerizes, and is able to stiffen and bridge DNA in the absence of magnesium (20). This indicates that these interactions indeed occur in the H-NS oligomer and their modulation by salt or mutagenesis induces a switch between its DNA binding modes.

To establish structure-function relationships for the MvaT protomer we investigated the effects of salt on the DNA binding properties of MvaT using TPM and a pull-down bridging assay.

MvaT, like H-NS, oligomerizes along the DNA substrate, leading to stiffening of DNA, in agreement with previous reports (38,39). Unlike H-NS, MvaT binds to the DNA substrate and induces bending. This is due to differences between the DNA binding mechanisms of the two proteins. MvaT binds to the DNA through an 'AT-pincer' motif which causes backbone bending (53). On the other hand H-NS binding to DNA involves an 'AT-hook like' structural motif (15,69) that intercalates within the DNA helix without perturbing its twist (70).

H-NS bridges are disrupted at lower KCl concentration compared to MvaT, indicating a higher sensitivity to the

ionic strength of the surrounding medium. These differences are likely due to differences in bridge stability resulting from the difference in DNA binding mechanisms, with MvaT forming a stronger bridge than H-NS. Additionally, H-NS requires a lower amount of $MgCl_2$ compared to MvaT to reach the maximum bridging activity (20). This could be explained by stronger electrostatic interdomain interactions within MvaT compared to H-NS, thus requiring higher KCl and $MgCl_2$ concentrations for their destabilization.

In contrast, StpA, an H-NS homologue, requires no or sub mM amounts of $MgCl_2$ to be able to bridge DNA (71,72). The high sensitivity of StpA towards magnesium chloride is possibly due to the weaker electrostatic interdomain interactions compared to H-NS and MvaT, as concluded from the charge distribution within its primary sequence (Supplementary Figure S1).

These three examples indicate that although the H-NS family members might structurally respond in a similar way to the increase in ionic strength to switch between their DNA stiffening and bridging activities, variations on this theme exist. These differences are due to the delicate divergence in their intrinsic charge distribution, and thus the fine-tuning of the strength of their electrostatic interdomain interactions.

The recently proposed mechanism by which H-NS senses temperature to alleviate gene repression involves unfolding of site 2, which induces an autoinhibitory conformational change within the H-NS protomer (25). Here we propose that H-NS family proteins do not require site 2 unfolding to sense the osmotic surrounding. Their osmosensitivity is mainly mediated by the modulation of the electrostatic interactions between their N-terminal and DNA binding domains within their nucleoprotein filaments. Altogether, we demonstrate that H-NS family protein nucleofilaments might respond differently to the environmental changes in temperature and ionic strength.

Thus, based on the description of the conformational landscape of MvaT, we propose a general mechanism for the basic response of H-NS family proteins to changes in osmotic environment (Figure 6). Under low ionic strength, the H-NS protomers interact individually with AT-rich nucleation sites on the DNA. From these sites, the protein spreads cooperatively along the DNA substrate forming lateral nucleoprotein filaments where only one of the DNA binding domains of each dimer is engaged with the DNA substrate. The other domain is sequestered by electrostatic interactions with the N-terminal domain. The DNA substrate and the increase in ionic strengths additively destabilize these interactions. Consequently, the protomers release their second DNA binding domains to interact with another DNA duplex and form a bridge. Above a certain threshold of ionic strength, the bridge is dissociated due to loss of the electrostatic interactions that mediate the complex. In addition, changes in DNA topology induced by salt (73) might contribute to formation or rupture of bridges.

Although there is to date no *direct* evidence for the occurrence of such mechanism in vivo, the ions investigated in this study are present in *E. coli* at different concentrations as a function of environmental conditions (74–76). For *P. aeruginosa*, limited information is available on the ionic composition of its intracellular milieu. However, in *E. coli* the cytosolic concentration of $K^+$ ranges from 30 to 300 mM and for $Cl^-$ from 10 to 200 mM (74,75), which correlates with the condition under which the MvaT protomers experience conformational changes between half-open and fully open states.

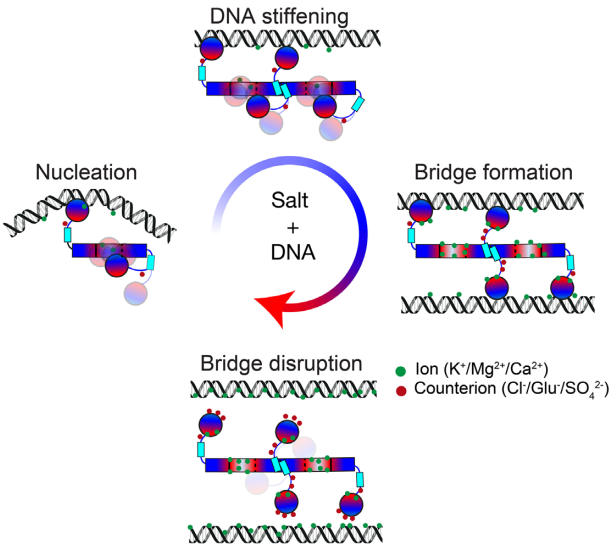


**Figure 6.** General mechanism of osmoregulation of the DNA binding properties of H-NS family proteins. The white, red and blue colors refer to neutral, negative and positive charged amino acid patch on the H-NS molecular surface.

In the present work, we have decrypted the molecular basis that governs DNA-DNA bridge formation by MvaT and proposed a structural dynamics paradigm for the osmosensitivity of H-NS family proteins. *In vivo* this mechanism is part of a more extensive and complex regulatory network. Clearly this process is modulated by other regulatory factors, such as protein modulators of H-NS function, ions and their cellular concentrations, in conjunction with local DNA topology. In addition to a fundamental understanding of the activities of H-NS family proteins, our findings pave the way for the modulation of their DNA binding modes by small chemical compounds as a new generation of antibiotics.

## DATA AVAILABILITY

The assignments of the MvaT F36D/M44D spectra are submitted to BMRB under the entry: 28010. The MvaT structural ensembles are submitted to SASDB with accession codes: SASDGS5 for MvaT (low salt) and SASDGT5 for MvaT (high salt).

## SUPPLEMENTARY DATA

Supplementary Data are available at NAR Online.

## ACKNOWLEDGEMENTS

We thank Dr Navraj Pannu for establishing the contact with Dr Gabriele Giachin at the European Synchrotron Radiation Facility to perform the SAXS experiment. Maud Bre-

mer is acknowledged for making the homology structural model of MvaT.

*Author contributions*: L.Q., F.B.B., G.G. and P.v.S. performed the experiments. L.Q., F.B.B., Y.G.J.S., A.N.V., J.V., G.G., M.U. and R.T.D. contributed to data analysis and discussion. F.B.B., M.U. and R.T.D. supervised the project. F.B.B. and R.T.D. wrote the manuscript. All authors reviewed and corrected the manuscript.

## FUNDING

Netherlands Organization for Scientific Research [VICI 016.160.613 to R.T.D.]; Human Frontier Science Program (HFSP) [RGP0014/2014 to R.T.D.]; China Scholarship Council (CSC) [201506880001 to L.Q.]. Funding for open access charge: Netherlands Organization for Scientific Research VICI Grant [016.160.613].

*Conflict of interest statement.* None declared.

## REFERENCES

1. Brooks,A.N., Turkarslan,S., Beer,K.D., Yin Lo,F. and Baliga,N.S. (2011) Adaptation of cells to new environments. *Wiley Interdiscip. Rev. Syst. Biol. Med.*, **3**, 544–561.
2. Krogh,T.J.T., Møller-Jensen,J.J. and Kaleta,C.C. (2018) Impact of chromosomal architecture on the function and evolution of bacterial genomes. *Front. Microbiol.*, **9**, 2019.
3. Dorman,C.J. (2004) H-NS: a universal regulator for a dynamic genome. *Nat. Rev. Microbiol.*, **2**, 391.
4. Tendeng,C. and Bertin,P.N. (2003) H-NS in Gram-negative bacteria: a family of multifaceted proteins. *Trends Microbiol.*, **11**, 511–518.
5. Atlung,T. and Ingmer,H. (1997) H-NS: a modulator of environmentally regulated gene expression. *Mol. Microbiol.*, **24**, 7–17.
6. Hurme,R. and Rhen,M. (1998) Temperature sensing in bacterial gene regulation—what it all boils down to. *Mol. Microbiol.*, **30**, 1–6.
7. Qin,L., Erkelens,A.M., Ben Bdira,F. and Dame,R.T. (2019) The architects of bacterial DNA bridges: a structurally and functionally conserved family of proteins. *Open Biol.*, **9**, 190223.
8. Ali,S.S., Xia,B., Liu,J. and Navarre,W.W. (2012) Silencing of foreign DNA in bacteria. *Curr. Opin. Microbiol.*, **15**, 175–181.
9. Navarre,W.W., McClelland,M., Libby,S.J. and Fang,F.C. (2007) Silencing of xenogeneic DNA by H-NS—facilitation of lateral gene transfer in bacteria by a defense system that recognizes foreign DNA. *Genes Dev.*, **21**, 1456–1471.
10. Lucchini,S., Rowley,G., Goldberg,M.D., Hurd,D., Harrison,M. and Hinton,J.C. (2006) H-NS mediates the silencing of laterally acquired genes in bacteria. *PLoS Pathog.*, **2**, e81.
11. Navarre,W.W., Porwollik,S., Wang,Y., McClelland,M., Rosen,H., Libby,S.J. and Fang,F.C. (2006) Selective silencing of foreign DNA with low GC content by the H-NS protein in *Salmonella*. *Science*, **313**, 236–238.
12. Singh,S.S., Singh,N., Bonocora,R.P., Fitzgerald,D.M., Wade,J.T. and Grainger,D.C. (2014) Widespread suppression of intragenic transcription initiation by H-NS. *Genes Dev.*, **28**, 214–219.
13. Oshima,T., Ishikawa,S., Kurokawa,K., Aiba,H. and Ogasawara,N. (2006) *Escherichia coli* histone-like protein H-NS preferentially binds to horizontally acquired DNA in association with RNA polymerase. *DNA res.*, **13**, 141–153.
14. Gordon,B.R., Li,Y., Cote,A., Weirauch,M.T., Ding,P., Hughes,T.R., Navarre,W.W., Xia,B. and Liu,J. (2011) Structural basis for recognition of AT-rich DNA by unrelated xenogeneic silencing proteins. *Proc. Natl. Acad. Sci. U.S.A.*, **108**, 10690–10695.
15. Bouffartigues,E., Buckle,M., Badaut,C., Travers,A. and Rimsky,S. (2007) H-NS cooperative binding to high-affinity sites in a regulatory element results in transcriptional silencing. *Nat. Struct. Mol. Biol.*, **14**, 441.
16. Rimsky,S., Zuber,F., Buckle,M. and Buc,H. (2001) A molecular mechanism for the repression of transcription by the H-NS protein. *Mol. Microbiol.*, **42**, 1311–1323.
17. Amit,R., Oppenheim,A.B. and Stavans,J. (2003) Increased bending rigidity of single DNA molecules by H-NS, a temperature and osmolarity sensor. *Biophys. J.*, **84**, 2467–2473.
18. Noom,M.C., Navarre,W.W., Oshima,T., Wuite,G.J. and Dame,R.T. (2007) H-NS promotes looped domain formation in the bacterial chromosome. *Curr. Biol.*, **17**, R913–R914.
19. Dame,R.T., Luijsterburg,M.S., Krin,E., Bertin,P.N., Wagner,R. and Wuite,G.J. (2005) DNA bridging: a property shared among H-NS-like proteins. *J. Bacteriol.*, **187**, 1845–1848.
20. van der Valk,R.A., Vreede,J., Qin,L., Moolenaar,G.F., Hofmann,A., Goosen,N. and Dame,R.T. (2017) Mechanism of environmentally driven conformational changes that modulate H-NS DNA-bridging activity. *Elife*, **6**, e27369.
21. Dame,R.T., Wyman,C., Wurm,R., Wagner,R. and Goosen,N. (2002) Structural basis for H-NS-mediated trapping of RNA polymerase in the open initiation complex at the rrnB P1. *J. Biol. Chem.*, **277**, 2146–2150.
22. Dame,R.T., Wyman,C. and Goosen,N. (2000) H-NS mediated compaction of DNA visualised by atomic force microscopy. *Nucleic Acids Res.*, **28**, 3504–3510.
23. Liu,Y., Chen,H., Kenney,L.J. and Yan,J. (2010) A divalent switch drives H-NS/DNA-binding conformations between stiffening and bridging modes. *Genes Dev.*, **24**, 339–344.
24. Winardhi,R.S., Yan,J. and Kenney,L.J. (2015) H-NS regulates gene expression and compacts the nucleoid: insights from single-molecule experiments. *Biophys. J.*, **109**, 1321–1329.
25. Shahul Hameed,U.F., Liao,C., Radhakrishnan,A.K., Huser,F., Aljedani,S.S., Zhao,X., Momin,A.A., Melo,F.A., Guo,X., Brooks,C. *et al.* (2018) H-NS uses an autoinhibitory conformational switch for environment-controlled gene silencing. *Nucleic Acids Res.*, **47**, 2666–2680.
26. Dorman,C.J., Hinton,J.C. and Free,A. (1999) Domain organization and oligomerization among H-NS-like nucleoid-associated proteins in bacteria. *Trends Microbiol.*, **7**, 124–128.
27. Rimsky,S. (2004) Structure of the histone-like protein H-NS and its role in regulation and genome superstructure. *Curr. Opin. Microbiol.*, **7**, 109–114.
28. Leonard,P.G., Ono,S., Gor,J., Perkins,S.J. and Ladbury,J.E. (2009) Investigation of the self-association and hetero-association interactions of H-NS and StpA from Enterobacteria. *Mol. Microbiol.*, **73**, 165–179.
29. Shindo,H., Iwaki,T., Ieda,R., Kurumizaka,H., Ueguchi,C., Mizuno,T., Morikawa,S., Nakamura,H. and Kuboniwa,H. (1995) Solution structure of the DNA binding domain of a nucleoid-associated protein, H-NS, from *Escherichia coli*. *FEBS lett.*, **360**, 125–131.
30. Esposito,D., Petrovic,A., Harris,R., Ono,S., Eccleston,J.F., Mbabaali,A., Haq,I., Higgins,C.F., Hinton,J.C. and Driscoll,P.C. (2002) H-NS oligomerization domain structure reveals the mechanism for high order self-association of the intact protein. *J. Mol. Biol.*, **324**, 841–850.
31. Bloch,V., Yang,Y., Margeat,E., Chavanieu,A., Augé,M.T., Robert,B., Arold,S., Rimsky,S. and Kochoyan,M. (2003) The H-NS dimerization domain defines a new fold contributing to DNA recognition. *Nat. Struct. Mol. Biol.*, **10**, 212.
32. Arold,S.T., Leonard,P.G., Parkinson,G.N. and Ladbury,J.E. (2010) H-NS forms a superhelical protein scaffold for DNA condensation. *Proc. Natl. Acad. Sci. U.S.A.*, **107**, 15728–11573.
33. Smyth,C.P., Lundbäck,T., Renzoni,D., Siligardi,G., Beavil,R., Layton,M., Sidebotham,J.M., Hinton,J.C., Driscoll,P.C. and Higgins,C.F. (2000) Oligomerization of the chromatin-structuring protein H-NS. *Mol. Microbiol.*, **36**, 962–972.
34. Renault,M., García,J., Cordeiro,T.N., Baldus,M. and Pons,M. (2013) Protein oligomers studied by solid-state NMR–the case of the full-length nucleoid-associated protein histone-like nucleoid structuring protein. *FEBS J.*, **280**, 2916–2928.
35. Westfall,L.W., Luna,A.M., San Francisco,M., Diggle,S.P., Worrall,K.E., Williams,P., Camara,M. and Hamood,A.N. (2004) The *Pseudomonas aeruginosa* global regulator MvaT specifically binds to the ptxS upstream region and enhances ptxS expression. *Microbiology*, **150**, 3797–3806.
36. Vallet,I., Diggle,S.P., Stacey,R.E., Cámara,M., Ventre,I., Lory,S., Lazdunski,A., Williams,P. and Filloux,A. (2004) Biofilm formation in

*Pseudomonas aeruginosa*: fimbrial cup gene clusters are controlled by the transcriptional regulator MvaT. *J. Bacteriol.*, **186**, 2880–2890.
37. Castang,S., McManus,H.R., Turner,K.H. and Dove,S.L. (2008) H-NS family members function coordinately in an opportunistic pathogen. *Proc. Natl. Acad. Sci. U.S.A.*, **105**, 18947–18952.
38. Castang,S. and Dove,S.L. (2010) High-order oligomerization is required for the function of the H-NS family member MvaT in *Pseudomonas aeruginosa*. *Mol. Microbiol.*, **78**, 916–931.
39. Winardhi,R.S., Fu,W., Castang,S., Li,Y., Dove,S.L. and Yan,J. (2012) Higher order oligomerization is required for H-NS family member MvaT to form gene-silencing nucleoprotein filament. *Nucleic Acids Res.*, **40**, 8942–8952.
40. Gibson,D.G., Young,L., Chuang,R.-Y., Venter,J.C., Hutchison,C.A. III and Smith,H.O. (2009) Enzymatic assembly of DNA molecules up to several hundred kilobases. *Nat. Methods*, **6**, 343.
41. van der Valk,R.A., Laurens,N. and Dame,R.T. (2017) *The Bacterial Nucleoid: Methods and Protocols*. In: Espéli,O (ed). Springer, NY, pp. 127–143.
42. van der Valk,R.A., Qin,L., Moolenaar,G.F. and Dame,R.T. (2018) *Bacterial Chromatin*. In: Dame,RT (ed). Springer, NY, pp. 199–209.
43. Pernot,P., Round,A., Barrett,R., De Maria Antolinos,A., Gobbo,A., Gordon,E., Huet,J., Kieffer,J., Lentini,M. and Mattenet,M. (2013) Upgraded ESRF BM29 beamline for SAXS on macromolecules in solution. *Synchrotron Radiat.*, **20**, 660–664.
44. Orthaber,D., Bergmann,A. and Glatter,O. (2000) SAXS experiments on absolute scale with Kratky systems using water as a secondary standard. *J. Appl. Crystallogr.*, **33**, 218–225.
45. Brennich,M.E., Kieffer,J., Bonamis,G., De Maria Antolinos,A., Hutin,S., Pernot,P. and Round,A. (2016) Online data analysis at the ESRF bioSAXS beamline, BM29. *J. Appl. Crystallogr.*, **49**, 203–212.
46. Petoukhov,M.V., Franke,D., Shkumatov,A.V., Tria,G., Kikhney,A.G., Gajda,M., Gorba,C., Mertens,H.D., Konarev,P.V. and Svergun,D.I. (2012) New developments in the ATSAS program package for small-angle scattering data analysis. *J. Appl. Crystallogr.*, **45**, 342–350.
47. Franke,D., Petoukhov,M., Konarev,P., Panjkovich,A., Tuukkanen,A., Mertens,H., Kikhney,A., Hajizadeh,N., Franklin,J. and Jeffries,C. (2017) ATSAS 2.8: a comprehensive data analysis suite for small-angle scattering from macromolecular solutions. *J. Appl. Crystallogr.*, **50**, 1212–1225.
48. Svergun,D. (1992) Determination of the regularization parameter in indirect-transform methods using perceptual criteria. *J. Appl. Crystallogr.*, **25**, 495–503.
49. Lee,W., Tonelli,M. and Markley,J.L. (2014) NMRFAM-SPARKY: enhanced software for biomolecular NMR spectroscopy. *Bioinformatics*, **31**, 1325–1327.
50. Vranken,W.F., Boucher,W., Stevens,T.J., Fogh,R.H., Pajon,A., Llinas,M., Ulrich,E.L., Markley,J.L., Ionides,J. and Laue,E.D. (2005) The CCPN data model for NMR spectroscopy: development of a software pipeline. *Proteins.*, **59**, 687–696.
51. Waudby,C.A., Ramos,A., Cabrita,L.D. and Christodoulou,J. (2016) Two-dimensional NMR lineshape analysis. *Sci. Rep.*, **6**, 24826.
52. Battiste,J.L. and Wagner,G. (2000) Utilization of site-directed spin labeling and high-resolution heteronuclear nuclear magnetic resonance for global fold determination of large proteins with limited nuclear overhauser effect data. *Biochemistry*, **39**, 5355–5365.
53. Ding,P., McFarland,K.A., Jin,S., Tong,G., Duan,B., Yang,A., Hughes,T.R., Liu,J., Dove,S.L. and Navarre,W.W. (2015) A novel AT-rich DNA recognition mechanism for bacterial xenogeneic silencer MvaT. *PLoS Pathog.*, **11**, e1004967.
54. Suzuki-Minakuchi,C., Kawazuma,K., Matsuzawa,J., Vasileva,D., Fujimoto,Z., Terada,T., Okada,K. and Nojiri,H. (2016) Structural similarities and differences in H-NS family proteins revealed by the N-terminal structure of TurB in *Pseudomonas putida* KT2440. *FEBS Lett.*, **590**, 3583–3594.
55. Schwieters,C.D., Kuszewski,J.J., Tjandra,N. and Clore,G.M. (2003) The Xplor-NIH NMR molecular structure determination package. *J. Magn. Reson.*, **160**, 65–73.
56. Schwieters,C.D., Kuszewski,J.J. and Clore,G.M. (2006) Using Xplor–NIH for NMR molecular structure determination. *Prog. Nucl. Magn. Reson. Spectrosc.*, **48**, 47–62.
57. Schwieters,C.D. and Clore,G.M. (2014) Using small angle solution scattering data in Xplor-NIH structure calculations. *Prog. Nucl. Magn. Reson. Spectrosc.*, **80**, 1–11.
58. Schwieters,C.D., Bermejo,G.A. and Clore,G.M. (2018) Xplor-NIH for molecular structure determination from NMR and other data sources. *Protein Sci.*, **27**, 26–40.
59. Tang,C., Iwahara,J. and Clore,G.M. (2006) Visualization of transient encounter complexes in protein–protein association. *Nature*, **444**, 383.
60. Pettersen,E.F., Goddard,T.D., Huang,C.C., Couch,G.S., Greenblatt,D.M., Meng,E.C. and Ferrin,T.E. (2004) UCSF Chimera—a visualization system for exploratory research and analysis. *J. Comput. Chem.*, **25**, 1605–1612.
61. Gao,Y., Foo,Y.H., Winardhi,R.S., Tang,Q., Yan,J. and Kenney,L.J. (2017) Charged residues in the H-NS linker drive DNA binding and gene silencing in single cells. *Proc. Natl. Acad. Sci. U.S.A.*, **114**, 12560–12565.
62. Shindo,H., Ohnuki,A., Ginba,H., Katoh,E., Ueguchi,C., Mizuno,T. and Yamazaki,T. (1999) Identification of the DNA binding surface of H-NS protein from *Escherichia coli* by heteronuclear NMR spectroscopy. *FEBS Lett.*, **455**, 63–69.
63. Fernández-de-Alba,C., Berrow,N.S., Garcia-Castellanos,R., García,J. and Pons,M. (2013) On the origin of the selectivity of plasmidic H-NS towards horizontally acquired DNA: linking H-NS oligomerization and cooperative DNA binding. *J. Mol. Biol.*, **425**, 2347–2358.
64. Micsonai,A., Wien,F., Bulyáki,É., Kun,J., Moussong,É., Lee,Y.-H., Goto,Y., Réfrégiers,M. and Kardos,J. (2018) BeStSel: a web server for accurate protein secondary structure prediction and fold recognition from the circular dichroism spectra. *Nucleic Acids Res.*, **46**, 315–322.
65. Eghbalnia,H.R., Wang,L., Bahrami,A., Assadi,A. and Markley,J.L. (2005) Protein energetic conformational analysis from NMR chemical shifts (PECAN) and its use in determining secondary structural elements. *J. Biomol. NMR.*, **32**, 71–81.
66. Clore,G.M. and Iwahara,J. (2009) Theory, practice, and applications of paramagnetic relaxation enhancement for the characterization of transient low-population states of biological macromolecules and their complexes. *Chem. Rev.*, **109**, 4108–4139.
67. Franke,D. and Svergun,D.I. (2009) DAMMIF, a program for rapid ab-initio shape determination in small-angle scattering. *J. Appl. Crystallogr.*, **42**, 342–346.
68. Worrall,J.A.R., Liu,Y., Crowley,P.B., Nocek,J.M., Hoffman,B.M. and Ubbink,M. (2002) Myoglobin and Cytochrome b5: A Nuclear Magnetic Resonance Study of a Highly Dynamic Protein Complex. *Biochemistry*, **41**, 11721–11730.
69. Gordon,B.R., Li,Y., Wang,L., Sintsova,A., van Bakel,H., Tian,S., Navarre,W.W., Xia,B. and Liu,J. (2010) Lsr2 is a nucleoid-associated protein that targets AT-rich sequences and virulence genes in *Mycobacterium tuberculosis*. *Proc. Natl. Acad. Sci. U.S.A.*, **107**, 200913551.
70. Huth,J.R., Bewley,C.A., Nissen,M.S., Evans,J.N., Reeves,R., Gronenborn,A.M. and Clore,G.M. (1997) The solution structure of an HMG-I (Y)–DNA complex defines a new architectural minor groove binding motif. *Nat. Struct. Mol. Biol.*, **4**, 657.
71. Lim,C.J., Whang,Y.R., Kenney,L.J. and Yan,J. (2011) Gene silencing H-NS paralogue StpA forms a rigid protein filament along DNA that blocks DNA accessibility. *Nucleic Acids Res.*, **40**, 3316–3328.
72. Boudreau,B.A., Hron,D.R., Qin,L., van der Valk,R.A., Kotlajich,M.V., Dame,R.T. and Landick,R. (2018) StpA and Hha stimulate pausing by RNA polymerase by promoting DNA-DNA bridging of H-NS filaments. *Nucleic Acids Res.*, **46**, 5525–5546.
73. Higgins,C.F., Dorman,C.J., Stirling,D.A., Waddell,L., Booth,I.R., May,G. and Bremer,E. (1988) A physiological role for DNA supercoiling in the osmotic regulation of gene expression in *S. typhimurium* and *E. coli*. *Cell*, **52**, 569–584.
74. Schultz,S.G., Wilson,N.L. and Epstein,W. (1962) Cation transport in *Escherichia coli*: II. Intracellular chloride concentration. *J. Gen. Physiol.*, **46**, 159–166.
75. Shabala,L., Bowman,J., Brown,J., Ross,T., McMeekin,T. and Shabala,S. (2009) Ion transport and osmotic adjustment in *Escherichia coli* in response to ionic and non-ionic osmotica. *Environ. Microbiol.*, **11**, 137–148.
76. Moncany,M. and Kellenberger,E. (1981) High magnesium content of *Escherichia coli* B. *Experientia*, **37**, 846–847.